MODELLING OF NECKING AND PRIMARY PARTICLE POLYDISPERSITY IN SOOT AGGREGATES AND THEIR EFFECTS ON THE SCATTERING MATRIX

by

Halil İbrahim Yazıcı

B.S., Mechanical Engineering, Boğaziçi University, 2020

B.S., Physics, Boğaziçi University, 2020

Submitted to the Institute for Graduate Studies in
Science and Engineering in partial fulfillment of
the requirements for the degree of
Master of Science

Graduate Program in Mechanical Engineering

Boğaziçi University

2023

ACKNOWLEDGEMENTS

I would like to express my gratitude to my supervisor, Prof. Hakan Ertürk, for the professional guidance he provided which made this work possible. Thanks to him, I had the chance to study and explore an important topic in nanotechnology which I find very interesting. I was able to overcome the challenges I faced through this study and develop a better understanding in regards to the related topics owing to his patience and faith in me. He also provided the opportunity for me to meet and collaborate with Dr. Fengshan Liu, who is an expert in the field of soot formation, morphology, and diagnostics. I would also like to thank Dr. Fengshan Liu for his professional guidance and valuable advice in regards to this work. Working with such successful and experienced researchers, I have gained a wider perspective on my thesis study which I will utilize in my next research studies as well.

I would like to thank to my family for their continuous support through this journey. My father, Eyüp, is the most determined and hardworking person I know. Being his son, I had no choice but to show the same amount of determination to my work. My mother, Bilgihan, has always been very supportive. I remember calling her on the way home at the times I was struggling with a lot of tasks and deadlines. Just to hear her voice would make me relieved and ready to attack on the tasks. I would like to thank my brothers, Abdurrahman and Yusuf Alp, for their support. The jogging and cross trainings that we went together were so enjoyable and refreshing. They helped me to increase my study efficiency. I would also like to thank the BU-TESLAB colleagues with whom we did enjoyable brain-storming sessions in regards to our research studies.

I would like to thank Boğaziçi University for support under B.U. Research Fund Grant Number 19144 and TÜBİTAK (Scientific and Technological Research Council of Turkey) for support under 2210-A program.

ABSTRACT

MODELLING OF NECKING AND PRIMARY PARTICLE POLYDISPERSITY IN SOOT AGGREGATES AND THEIR EFFECTS ON THE SCATTERING MATRIX

Soot has complex morphological characteristics such as aggregate and primary particle polydispersity, and necking. Modelling these structures and their effects on the optical behavior is challenging attributed to the complex morphology and the corresponding formation mechanism. In this study, a comprehensive analysis of the impacts of necking and polydispersity in aggregate and primary particle size is conducted to identify their effects on scattering matrix elements. Aggregate representations are generated via tunable fractal generation algorithms using particle-cluster and cluster-cluster aggregation, based on typical morphological parameters of flame-soot. Different necking models are evaluated quantitatively based on measured scattering matrix elements derived from an experimental study in the literature. Polydispersity in aggregate and primary particle size are implemented through log-normal distribution functions. Scattering matrix elements are calculated via discrete dipole approximation and multi-sphere T-matrix method. The impacts of the considered structures on the scattering matrix elements are presented, and the volume variation-based approach is evaluated for representing the impact of necking. According to the results, the impacts of necking and primary particle polydispersity are similar and dominated by the resultant volume change, whereas that of aggregate polydispersity is more complicated. Accordingly, the volume variation-based approach performs well in representing the effect of necking on the scattering matrix for the specified cases. The deficiency of the volume variation-based approach is discussed as well, and an enhancement is proposed to increase its accuracy.

ÖZET

KURUM PARÇACIK TOPLULUKLARINDA BOYUNLANMA İLE TOPLULUK VE BİRİNCİL PARÇACIK POLİDİSPERSİTESİNİN VE SAÇILMA MATRİSİ ÜZERİNDEKİ ETKİLERİNİN MODELLEMESİ

Kurum, parçacık topluluğu ve birincil parçacık polidispersitesi ile boyunlanma gibi karmaşık morfolojik özelliklere sahiptir. Bu yapıları ve bunların optik özellikler üzerindeki etkilerini modellemek, morfolojinin ve ilgili formasyon mekanizmalarının karmaşıklığından dolayı zorlu bir iştir. Bu çalışmada, boyunlanma ile topluluk ve birincil parçacık boyutundaki polidispersitenin etkileri saçılma matris elemanları üzerindeki etkileri baz alınarak kapsamlı bir şekilde analiz edilir. Topluluk modelleri, alev kurumunun tipik morfolojik parametrelerini baz alarak ayarlanabilir fraktal oluşturma algoritmalarıyla parçacık-küme ve küme-küme toplanması kullanılarak üretilir. Farklı boyunlanma modelleri, literatürdeki deneysel bir çalışmadan elde edilen saçılma matrisi ölçümlerine dayalı nicel olarak değerlendirilir. Topluluktaki ve birincil parçacık boyutundaki polidispersite, log-normal dağılım fonksiyonları ile modellenir. Saçılma matrisi elemanları, ayrık dipol yaklaşımı ve çok küreli T-matris yöntemi ile hesaplanır. Ele alınan yapıların saçılma matrisi üzerindeki etkileri sunulur ve boyunlanmanın etkisini temsil etmek için önerilen hacim değişimine dayalı yaklaşım değerlendirilir. Sonuçlara göre, boyunlanma ve birincil parçacık polidispersitesinin etkileri benzerdir ve büyük oranda hacim değişikliği ile ilişkilidir, ancak topluluk polidispersitesinin etkileri daha karmaşıktır. Hacim değişimine dayalı yaklaşım belirtilen durumlar için boyunlanmanın saçılma matrisine etkisini temsil etmede iyi performans göstermiştir. Hacim değişimine dayalı yaklaşımın eksikliği de tartışılmış, doğruluğunu artırmak için bir geliştirme önerilmiştir.

TABLE OF CONTENTS

LIST OF FIGURES

LIST OF TABLES

LIST OF SYMBOLS

C	Conversion factor between mobility diameter and volume equivalent diameter of aggregates
C_{neck}	Necking coefficient
C_{sca}	Scattering cross-section
d	Dipole separation distance
D_f	Fractal dimension
d_{mob}	Mobility diameter of an aggregate
d_p	Primary particle diameter
$d_{p,g}$	Geometric mean of primary particle diameter distribution
d_{ve}	Volume equivalent diameter of an aggregate
g	Asymmetry factor
I	First element of the Stokes vector
k	Wavenumber
k_f	Fractal pre-factor
m	Refractive index
m_{agg}	Mass of the aggregate
m_{pi}	Mass of the i^{th} primary particle
n	Number fraction
N_p	Number of particle in an aggregate
p	Log-normal probability distribution
Q	Second element of the Stokes vector
R	Ratio of Cunningham slip correction factors of d_{mob} and d_{ve}
r	Distance between the aggregate and detector
r_{con}	Radius of the cylindrical connector
R_g	Radius of gyration of the aggregate
r_{gi}	Radius of gyration of the i^{th} primary particle
R_i	Distance of the center of the i^{th} primary particle from the center of mass of the aggregate

r_p	Primary particle radius
r_{pi}	Radius of the i^{th} primary particle
S	Scattering matrix
S_{ij}	Element of S in the i^{th} row and j^{th} column
S^{au}	Scattering matrix (arbitrary units - a.u.)
S_{ij}^{au}	Element of S^{au} in the i^{th} row and j^{th} column
U	Third element of the Stokes vector
V	Fourth element of the Stokes vector
Δ	Linear depolarization ratio
θ	Scattering angle
λ	Wavelength
μ	Arithmetic mean
μ_g	Geometric mean
μ_{g,d_p}	Geometric mean of primary particle diameter distribution
μ_{g,N_p}	Geometric mean of the distribution of number of particles in an ensemble of aggregates
σ	Normal standard deviation
σ_g	Geometric standard deviation
σ_{g,d_p}	Geometric standard deviation of primary particle diameter distribution
σ_{g,N_p}	Geometric standard deviation of the distribution of number of particles in an ensemble of aggregates
χ	Dynamic shape factor of soot
ψ	Scalar function defining the level-set function model

LIST OF ACRONYMS/ABBREVIATIONS

3D	Three Dimensional
CAVA	Constant Aggregate Volume Approach
CCA	Cluster-cluster Aggregation
CMRA	Constant Monomer Radius Approach
DDA	Discrete Dipole Approximation
DLA	Diffusion Limited Aggregation
FLAGE	Fractal-like Aggregate Generation Environment
LFM	Level-set Function Model
MALS	Multi Angle Light Scattering
MCCM	Modified Cylindrical Connector Model
MSTM	Multi-sphere T-matrix Method
NRMSE	Normalized Root-mean-square Error
PCA	Particle-cluster Aggregation
RDG	Rayleigh-Debye-Gans
RDG-FA	Rayleight-Debye-Gans for Fractal Aggregates
RLA	Reaction Limited Aggregation
SEM	Scanning Electron Microscopy
TEM	Transmission Electron Microscopy
TR-LII	Time Resolved Laser-induced Incandescence

1. INTRODUCTION

Combustion systems have certain adverse effects on human health [1, 2] and the environment [3, 4] arising from emission of particulates produced by incomplete combustion of hydrocarbon fuels. Soot is one of the major emitted particulates and consists of aggregated carbonaceous nanoparticles exhibiting a fractal-like structure. Identification of morphological properties associated with soot aggregates is necessary since these properties are directly related to the formation, transport, and physical properties of the produced nanostructures. These properties provide information on the combustion process, and the environmental and health impacts of combustion emissions. Accordingly, the morphological information of soot aggregates might be used to make regulations on the combustion systems for improving the combustion efficiency and reducing the damages to the environment and human health. Researchers have been trying to develop in-situ diagnostic methods for morphology of combustion-generated nanostructures to identify their physical properties without disturbing the production process and possibly introducing errors in diagnostics associated with sampling. The in-situ diagnostic methods for soot aggregates require to solve the inverse problem of deriving the morphological parameters of aggregates based on observed physical behaviour. Therefore, these methods rely on accurate representation of morphology so that the physical behavior associated with the nanostructures can be accurately modeled.

Optical properties are frequently utilized in developing in-situ characterization methods for soot aggregates. Frequently employed characterization methods for soot rely on time-resolved laser induced incandescence (TR-LII) [5] and multi-angle light scattering (MALS) [6, 7]. The TR-LII method relies on inferring the primary particle size from the temporal change in the incandescence signal of the heated aggregate structure to incandescent temperatures via a laser pulse. MALS-based characterization is to infer the morphological parameters of the aggregate based on its light scattering profile when illuminated by a laser. There are some advantages of MALS based methods,

mainly due to enabling in-situ characterization of aggregates consisting of both absorbing and non-absorbing materials. Moreover, the polarization states of the incident and scattered light might be altered via implementing polarizers to obtain comprehensive information on the morphology of the aggregates.

Accurate representation of dependence of optical behavior on morphology is critical as the accuracy and reliability of the characterization relies on it. Moreover, the morphological structure associated with soot should be known adequately to improve the fidelity of the analysis. Morphological characteristics of various soot samples are investigated in the literature based on electron microscopy images (TEM/SEM). These studies demonstrated macro and micro structural characteristics of soot aggregates. Electron microscopy images of various flame-soot samples demonstrated that the aggregate size exhibit a non-uniform distribution that can be fitted to a log-normal distribution [8, 9]. On the other hand, certain micro-structural effects such as primary particle polydispersity, necking between neighboring primary particles, and overlapping are also present in soot aggregates [10–14]. Modelling all these structural effects is challenging due to the complexity of physics of their formation mechanism and this complicates the prediction of the scattering properties considering them.

The accuracy of MALS-based optical characterization depends on the numerical scattering model representing the complex relationship between the morphology and the scattering properties of the aggregate. The accuracy of the numerical scattering model is dependent on the fidelity of the scattering simulations and the aggregate representations. Scattering simulations are performed based on numerically generated aggregate representations to calculate the scattering properties. Scattering simulations are frequently conducted via approximations such as Rayleigh-Debye-Gans Theory for Fractal-Aggregates (RDG-FA) [15], Multi-Sphere T-matrix Method (MSTM) [16], and Discrete Dipole Approximation (DDA) [17]. While RDG-FA is much easier to implement for scattering property calculations, it fails to account for the multiple scattering events within the aggregate [18], which might lead to significant errors. MSTM is an analytical method developed by Mackowski and Mishchenko [16] to calculate the

orientation-averaged scattering matrix and total cross-sections for arbitrary cluster of spherical particles. However, it assumes that the primary particles are non-overlapping perfect spheres that limits its use to idealized aggregates. In DDA, the aggregate is represented by a large number of discrete polarizable points referred as dipoles [17]. Although DDA accounts for the multiple scattering effects and can calculate scattering properties of aggregates of complex geometries even with microstructural effects, its prediction accuracy depends on the number of discrete points, which has a direct impact on the computational load.

Each structural effect has a distinctive impact on the optical behavior of the aggregate that might be significant depending on the extend of the corresponding structure. There are certain studies in the literature on the effect of aggregate and primary particle size polydispersity on the radiative properties of soot aggregates. Farias et al. [19] conducted a numerical study on the effects of aggregate and primary particle polydispersity on radiative properties of soot aggregates. They used log-normal distribution to implement polydispersity in aggregate size, and normal distribution to implement polydispersity in primary particle size. The impact of aggregate polydispersity on the scattering properties was observed to be more pronounced than that of primary particle polydispersity, whereas the corresponding impacts on the absorption cross-section were comparable [19]. Charalampopoulos and Shu [20] studied the effects of aggregate and primary particle polydispersity on light scattering properties of chain-like soot aggregates. They used log-normal distribution to implement polydispersity in aggregate and primary particle size. The geometric mean and standard deviation associated with aggregate size distribution were found to be relatively small compared to [19]. Contrary to [19], the effect of primary particle polydispersity on the light scattering quantities was observed to be more significant than that of aggregate polydispersity [20]. F. Liu et al. [21] investigated the impacts of polydispersity of aggregate and primary particle size distributions on temperature of soot aggregates in low-fluence laser-induced incandescence. Log-normal distribution is used to introduce polydispersity in aggregate and primary particle size. They concluded that the impact of primary particle polydispersity is important and should be implemented in the aggregate model [21]. However,

the significance of the influence of aggregate polydispersity on the temperature of soot was observed to be dependent on the heat conduction regime [21].

There are also studies in the literature studying the effect of minor structures such as primary particle polydispersity and necking on the radiative properties of soot aggregates. C. Liu et al. [22] investigated the influence of primary particle size distribution on the radiative properties of soot aggregates. They concluded that primary particle polydispersity needs to be considered to achieve more accurate understanding of the relation between morphology and radiative properties [22]. Bescond et al. [14] conducted a study on inferring the primary particle size distribution of soot aggregates with necking and overlapping based on light depolarization measurements. Their work indicated that the impact of necking on the light depolarization ratio is more enhanced relative to that of overlapping [14]. Skorupski and Mroczka [23] investigated the effect of necking and polydispersity on the integral optical properties of soot aggregates and observed that these structures have significant impacts. Yon et al. [24] studied the influence of necking and overlapping on the radiative properties of soot and concluded that the corresponding effects are considerable. Teng et al. [25] considered the optical properties of soot aggregate representations with minor structures such as necking, polydispersity, and coating. The effect of necking on the optical properties was shown to be more significant as compared to the other structures [25].

According to the literature, the minor structures of soot aggregates such as necking and primary particle polydispersity have considerable impacts on certain radiative properties, and accurate prediction of these properties necessitates the proper representation of these structures. J. Liu et al. [26] compared the normalized bulk scattering matrix elements obtained from experimental measurements and numerical predictions by MSTM. They observed remarkable deviations between the experimental and numerical results for specific normalized Mueller matrix elements especially for S_{22}/S_{11} and S_{34}/S_{11}, and suggested that introducing minor structures such as necking and overlapping to the aggregate representations might reduce these deviations [26]. Talebi-Moghaddam et al. [6] developed a method of optical characterization of soot via

Bayesian inference using an artificial neural network surrogate model that is trained with data generated by MSTM. They observed deviations between the predicted and TEM-derived fractal parameters, and stated that neglecting necking might be one of the main causes of these deviations [6]. Available studies investigating the effects of minor structures on the radiative and optical properties of soot aggregates conclude that necking has a significant impact on the optical properties of soot aggregates [14,25] and introducing necking to the aggregate models might improve the accuracy of models used for optical characterization of soot. Therefore, the effect of necking on the optical properties should be further investigated.

There are different approaches to model necking between primary particles in soot aggregates. While Bescond et al. [14] and Yon et al. [24] used 3D level-set function to represent necking, Skorupski and Mroczka [23] modeled necking between particles using simpler structures such as cylindrical, linear, and quadratic connectors. Similarly, Teng et al. [25] used cylindrical connectors to represent necking between primary particles of black carbon aerosols. Whereas, Bao et al. [27, 28] represented necking via ball-shaped connectors. On the other hand, the studies by Skorupski and Mroczka [23], Teng et al. [25], and Bao et al. [27, 28] considered monodisperse aggregates whereas Bescond et al. [14] and Yon et al. [24] considered necking in polydisperse aggregates. Therefore, there is no unified approach for modeling soot aggregates with necking effect. Besides, no simpler necking model is considered for polydisperse aggregates as an alternative to the 3D level-set function model defined by Bescond et al. [14]. Moreover, these necking models are not evaluated by comparison with experimental data due to limited experimental data in the literature. However, recent improvements in diagnostics enable such experiments and J. Liu et al. [26] recently presented full scattering matrix measurements of re-aerosolized toluene and n-heptane soot, together with their analyses using MSTM.

Alternatively, simplified approaches are proposed to resemble the effect of primary particle polydispersity and necking on the optical behavior to overcome the challenges with modelling these structures. F. Liu et al. [21] generated aggregates formed by

monodisperse primary particles based on the Sauter mean diameter so that the effect of monomer polydispersity is represented based on the corresponding change in the aggregate surface area. C. Liu et al. [22] used geometric mean and volume mean diameter based approaches to generate aggregates formed by monodisperse primary particles. They compared the resultant optical properties associated with these aggregates and aggregates formed by polydisperse primary particles. It was found that the volume mean diameter approach yielded more accurate estimations of integral optical properties such as extinction and absorption cross-sections [22]. Whereas, the geometric mean diameter based approach performed better in estimating the phase matrix elements [22]. Yon et al. [29] studied the influence of primary particle polydispersity on the radiative properties of soot aggregates. They used volume mean diameter approach with RDG-FA and observed that it results in sufficiently accurate approximations for the scattering and absorption cross-sections [29]. Teng et al. [25] presented a unified approach to account for the effect of minor structures such as necking and polydispersity on the optical properties based on the resultant change in the aggregate volume. They demonstrated that the impact of the minor structures on the optical behavior is substantially related to the resultant volume variation [25]. However, impacts of the minor structures are limited such that the resultant volume change is not larger than 20%. This constraint might result in underestimation of the potential effects of these structures. Considering the literature, more comprehensive studies are required to determine the accuracy of the volume variation based approach in representing the effect of primary particle polydispersity and necking.

The effects of morphological characteristics are generally investigated over the integral properties such as extinction, absorption, and scattering cross-section and/or specific combinations of the normalized phase matrix elements. However, these properties might be misleading due to the loss of morphological information associated with integration and/or normalization. Alternatively, identifying their impacts based on the overall scattering matrix elements might provide more comprehensive information. Considering the physical meanings of elements of the scattering matrix, they might provide more detailed knowledge on the influence of different morphological charac-

teristics on the optical behavior. Accordingly, the relation between morphology and scattering properties of soot aggregates can be established more accurately.

In the literature, elliptically polarized light scattering experiments are utilized to infer morphological characteristics of different nanoparticles. Manickavasagam et al. [30] presented the scattering matrix element profiles for ellipsoidal and cylindrical particles with different aspect ratios. They stated that the elements, S_{12} and S_{34}, exhibited more pronounced sensitivity to the particle shape as compared to S_{11}, where the latter is observed to be the most shape-sensitive element. Aslan et al. [31] utilized elliptically polarized light scattering technique to determine the shape and size of colloidal metal oxide particles based on different scattering matrix elements. Accordingly, polarized light scattering is expected to yield comprehensive information on the morphology of aggregates including minor structures based on the overall scattering matrix elements. Experimental methods proposed to measure the optical properties of different particles for characterization purposes are summarized by M. P. Menguc [32], including the experimental techniques utilized in polarized light scattering experiments. Experimental apparatus described in [33,34] can be used to conduct polarized light experiments on soot samples to infer comprehensive information on their morphology.

Moreover, there are studies in the literature utilizing specific scattering matrix elements for developing in-situ optical characterization methods for soot aggregates [6,7,35–37]. Accurate knowledge of the influence of morphological characteristics of soot on the scattering matrix is essential for these studies. Teng et al. [25] considered the effect of necking with other minor structural defects on bulk optical properties and the scattering matrix. They presented numerical results obtained from DDA for the aggregate representations including distinct minor structures and the ideal aggregates without any microstructural effects. The minor structures were quantified through the resultant relative volume difference between an aggregate with minor structures and the corresponding ideal aggregate. Thus, the relative effects of distinct microstructures on the optical properties were compared for the same resultant changes in the aggregate volume. They concluded that the effect of minor structures on the scattering matrix is

negligibly small. However, they limited the relative volume difference between aggregates with minor structures and the ideal aggregate to 0.1, which imposes a restriction on the degree of necking. As a result, this approach might lead to an underestimation of the impact of necking. Moreover, it is not possible to comprehend the real effect of necking on the scattering matrix in terms of predicting the measurement data since no experimental data were considered in their study.

In this study, a comprehensive analysis of the effect of necking and polydispersity in aggregate and primary particle size in soot is conducted based on the resultant scattering matrix elements. In order to identify a unified representation approach for necking it is necessary to study different models proposed in the literature. Therefore, evaluation of different models of necking in soot aggregates based on light scattering measurements must be carried out to establish a unified methodology for generating realistic aggregate representations. To this end, a quantitative analysis of different necking models in estimating the scattering matrix for the soot aggregates reported by J. Liu et al. [26] is conducted. The 3D level-set function model (LFM) [14, 24] and modified cylindrical connector model (MCCM) are used to introduce necking for both monodisperse and polydisperse aggregate representations. The performance of each model is evaluated through comparisons of the estimated scattering matrix elements with those of measurements by J. Liu et al. [26]. Through this approach, this study also provides a methodology for quantitative comparison of different necking models in representing necking in soot aggregates based on experimental measurements of their optical properties. Moreover, this study contributes to developing a better understanding of the relation between morphology and optical properties of soot aggregates which is essential for in-situ optical diagnostics. Additionally, the accuracy of the volume variation based approach proposed for approximating the effect of primary particle polydispersity and necking on the optical behavior is comprehensively investigated based on the scattering matrix.

2. THEORY

2.1. Fractal Aggregate Representation

The numerical aggregation models imitate the formation of fractal-like aggregates in nature. These pseudo models utilize two main algorithms that are particle-cluster aggregation (PCA) and cluster-cluster aggregation (CCA) algorithms. PCA algorithm relies on attaching a new primary or monomer particle to the cluster of particles at each step of aggregation [38]. Whereas, CCA algorithm is based on combining the clusters of similar size with each other rather than combining primary particles with the growing cluster [38].

The fractal-like structure of real aggregates can be described by the statistical scaling law defined as

$$N_p = k_f \left(\frac{R_g}{\bar{r}_p} \right)^{D_f} \tag{2.1}$$

where N_p is the number of particles, $\bar{r}_p$ is the mean particle radius in the aggregate, R_g is the radius of gyration of the aggregate, k_f and D_f are the fractal parameters referred as fractal pre-factor and fractal dimension, respectively [15]. While the statistical scaling law is valid for averaged characteristic parameters, the distribution of each parameter might be affected by conditions of aggregate formation in a particular way, which is challenging to identify. Therefore, it is reasonable to assume that these distributions are Dirac delta distributions such that the scaling law holds for each individual aggregate.

Diffusion limited aggregation (DLA) and ballistic aggregation are commonly used models in representing the mechanism of aggregation of soot for both PCA and CCA. Although they approximate the aggregation mechanism, the fluctuations in the fractal parameters derived from the statistical scaling law are considerable [39]. These fluctuations should be dampened to obtain more stable and reliable aggregate representations

that approximate the real structure based on its fractal parameters derived from the statistical scaling law. There are alternative algorithms that are tunable based on the statistical scaling law utilizing PCA and CCA, and preserve the prescribed fractal parameters. Filippov et al. [39] developed fractal generation algorithms based on both PCA and CCA, in which the fractal parameters are exactly preserved at each step of aggregation. Even though the tunable PCA algorithm is fast and easy to implement, it might yield structures that do not mimic the real aggregates [39]. While the tunable CCA algorithm yields more realistic structures, creating aggregates with large D_f values might be problematic [39].

The algorithms developed by Filippov et al. [39] can be used to generate aggregates formed by monodisperse primary particles only. However, these algorithms might be modified to generate aggregates formed by polydisperse primary particles as well, as formulated by Skorupski et al. [40]. Skorupski et al. [40], suggested a fast and accurate implementation of tunable fractal-like aggregate generation algorithms based on various methods such as DLA, RLA, ballistic aggregation, and Filippov's algorithm [39]. They developed a fractal-like aggregate generation software, FLAGE, consisting of different aggregation methods based on both PCA and CCA used to generate aggregate structures according to predefined fractal parameters. Although FLAGE is a fast and accurate tool for fractal representation, it might not exactly preserve the predefined fractal parameters for each aggregate, especially for aggregates formed by polydisperse primary particles [41]. FracVAL is an alternative software developed by Moran et al. [41] to generate fractal-like structures representing aggregates consisting of polydisperse primary particles based on CCA. It utilizes the mass of primary particles to modify Filippov's original CCA algorithm [39] for generating aggregates formed by polydisperse primary particles based on the modified fractal law suggested by Dastanpour et al. [42]. It yields fractal parameters with a narrower distribution around the prescribed values as compared to the modified Filippov's CCA algorithm proposed by Skorupski et al. [40]. However, convergence might be an issue for CCA-based fractal representation tools such as FracVAL. Optimizing the accuracy and execution time is crucial while making the choice of appropriate aggregate representation method for a

specific study. Therefore, the identification of the optimum tool for aggregate representation should be conducted primarily considering the characteristic parameters derived from the images associated with the real aggregates of interest.

2.2. Scattering Matrix

Scattering matrix relates the Stokes vectors associated with the incident and scattered beams of light defined with respect to the scattering plane. There are two distinct definitions of the scattering matrix. The first definition is given as

$$\begin{bmatrix} I_\lambda(\theta) \\ Q_\lambda(\theta) \\ U_\lambda(\theta) \\ V_\lambda(\theta) \end{bmatrix}_{sca} = \frac{1}{k^2 r^2} \begin{pmatrix} S_{11} & S_{12} & S_{13} & S_{14} \\ S_{21} & S_{22} & S_{23} & S_{24} \\ S_{31} & S_{32} & S_{33} & S_{34} \\ S_{41} & S_{42} & S_{43} & S_{44} \end{pmatrix} \begin{bmatrix} I_\lambda(\theta) \\ Q_\lambda(\theta) \\ U_\lambda(\theta) \\ V_\lambda(\theta) \end{bmatrix}_{inc} \tag{2.2}$$

where I, Q, U, and V are the Stokes parameters indicating unpolarized, linearly, obliquely, and circularly polarized intensities, respectively. Here, subscripts *sca* and *inc* refer to scattered and incident beams, respectively, k is the wavenumber, r is the distance between the detector and the target object, and S_{ij} are the elements of the scattering matrix.

A normalized scattering matrix is obtained via multiplying the scattering matrix defined in Equation (2.2) with the scaling factor, $C_{\lambda,sca}k^2/4\pi$ so that the integration of the element in the first row and the first column over all scattering angles gives unity. The elements of the normalized scattering matrix as defined are indicated with the superscript, au, as S_{ij}^{au}.

The scattering matrix might be simplified for macroscopically isotropic and symmetric structures, in which all orientations of the target are equally probable and there exists a plane of symmetry for each particle, and/or there are equal number of particles and their mirror counterparts in the target structure [43]. Accordingly, nanoparticle

aggregates consisting of a large cluster of randomly oriented particles can be considered as macroscopically isotropic and symmetric structures [44]. In this case, Equation (2.2) reduces to the block-diagonal form given as

$$\begin{bmatrix} I \\ Q \\ U \\ V \end{bmatrix}_{sca} = \frac{1}{k^2 r^2} \begin{pmatrix} S_{11} & S_{12} & 0 & 0 \\ S_{12} & S_{22} & 0 & 0 \\ 0 & 0 & S_{33} & S_{34} \\ 0 & 0 & -S_{34} & S_{44} \end{pmatrix} \begin{bmatrix} I \\ Q \\ U \\ V \end{bmatrix}_{inc} \tag{2.3}$$

for a specific set of (λ, θ) [43, 45].

There are only six nonzero independent scattering matrix elements in Equation (2.3) for fractal-like aggregate structures. Each of these elements and/or their combinations are related to one or more characteristic properties of the aggregate in a specific manner. These matrix elements might be utilized separately in characterization of the aggregate structure in terms of different morphological properties such as shape, size distribution, and compactness considering their correlation with these properties.

S_{11} is known to be the differential scattering cross-section associated with the target object [46]. It relates unpolarized scattered intensity with unpolarized incident light intensity and it is sensitive to both N_p and r_p [46]. Therefore, it might be used in characterization of size distribution and number of primary particles in the aggregate. Ericok et al. [7, 35–37] showed prediction on N_p and r_p for soot characterization using unpolarized intensity measurements. Although S_{11} provides useful information about the size of the primary particles and the aggregate, it might not be sufficient for providing comprehensive information on the morphological structure of the aggregate by itself [46].

The trend of S_{12} is highly dependent on r_p while the value of the extremum is proportional to N_p [46]. Therefore, S_{12} might provide more accurate size distribution when combined with S_{11}. It is also sensitive to primary particle polydispersity, number

of orientations used in the numerical simulations, fractal dimension D_f, and deviations from the Rayleigh-Debye-Gans (RDG) theory [44, 46]. Moreover, the ratio, $-S_{12}/S_{11}$, is related to the linear polarization ratio, which denotes the portion of unpolarized incident intensity that is linearly polarized after scattering from the target object. Therefore, it might contain further information about the morphology of the structure which can be useful in characterization applications.

S_{22} is known to be highly sensitive to the shape of the particles [14]. It is referred as a measure of sphericity of particles and approaches unity for the limiting case of a perfect sphere [45]. Furthermore, it is related to the "linear depolarization ratio", Δ, through $\Delta = 1 - S_{22}/S_{11}$. Considering physical meaning of S_{22} and/or S_{22}/S_{11}, and their correlation with the shape of particles, S_{22} is an important candidate for characterization of minor structures such as necking, overlapping, and irregularities in the aggregates.

While S_{33} and S_{44} have similar trends depending on r_p and N_p, they might also provide information on the asymmetry of the structure through the ratio of total scattered intensities at forward to backward scattering angles. They might be used in deriving information on the shape of the aggregate as well as r_p and N_p; however, their contribution to the accuracy of characterization should be identified.

S_{34} is associated with the measure of circularly polarized scattered light when the incident light is obliquely polarized ($\pm 45°$) [46]. S_{34} is sensitive to the fractal dimension, D_f, such that it increases with increasing D_f [47] and also depends on the shape, compactness, and granularity of the aggregate [46]. Moreover, it is sensitive to the polydispersity of primary particles, number of orientations in numerical simulations, and deviations from RDG theory as S_{12} [45, 46]. Although S_{34} has certain unique features that might be utilized in characterization of aggregates, its relatively small values are prone to measurement uncertainties affecting the accuracy of characterization.

3. PROBLEM DESCRIPTION

Some of the morphological characteristics of soot that exhibit significant impact on the optical properties are necking and polydispersity in aggregate and monomer size. This study investigates the effect of these characteristics on the scattering matrix elements, S and S^{au}, to develop a comprehensive understanding on the relation between morphology and optical behavior. Considering that there is no unified approach for representing necking in soot aggregates, a preliminary study on quantitative analysis of different necking models is conducted. Accordingly, there are two main problems addressed in this work, which are described in Sections 3.1 and 3.2 in detail.

3.1. Quantitative Analysis of Different Necking Models in Predicting the Scattering Matrix

This preliminary study aims at identifying the proper model that adequately represents necking in soot aggregates as far as their scattering behavior is concerned. Necking is implemented to the monodisperse and polydisperse aggregate representations via different models in the literature. The method used for representing necking might have an effect on optical properties of soot aggregates. Accordingly, the lack of knowledge on the proper necking model might introduce errors to the optical characterization methods.

To identify the proper necking model, optical properties estimated numerically for aggregate representations including necking implemented with different models are compared with experimental measurements. The full set of non-zero scattering matrix elements is considered as it contains the maximum information related with the morphology of the soot aggregates. The study by J. Liu et al. [26] provides both experimental and numerical simulation results associated with the complete set of normalized non-zero scattering matrix elements for soot produced in toluene and n-heptane diffusion flames. The presented scattering matrix elements are normalized over the bulk

values obtained for samples of toluene and n-heptane soot whose size distributions were also measured and provided by [26]. The measured and estimated scattering matrix elements by MSTM, and aggregate size distribution associated with the toluene soot samples are presented in [26]. It can be seen in [26] that the differences between measurements and simulation results become more pronounced for $\widetilde{\langle S_{22} \rangle}$ and $\widetilde{\langle S_{34} \rangle}$, where $\widetilde{\langle S \rangle}$ represents the normalized scattering matrix elements. These elements are known to be sensitive to shape and morphological properties of the aggregates such as compactness and granularity. Therefore, the authors recommended that the impact of introducing minor structures such as necking and overlapping to the numerical aggregate models on reducing the deviations for these specific normalized scattering matrix elements should be investigated [26].

In this preliminary study, the effects of necking on both normalized and bulk scattering matrix element data are investigated for toluene soot samples with the TEM-derived morphological properties given in Table 3.1 below [26]. Note that the parameters related with the primary particle size in the soot samples include the surface growth of soot particles arising in the process of soot formation and sampling. Governing mechanisms are surface reactions, sintering, and condensation of particulate matter such as polycyclic hydrocarbons onto soot particles [48]. Accordingly, primary particle sizes are enlarged as compared to early-stage soot particles. The fractal parameters are considered as $D_f = 2.16$ and $k_f = 2.62$, and kept constant for this study considering that this configuration yielded satisfactory agreement with the experimental data. Besides, the effect of fractal parameters in the range specified in Table 3.1 exhibited a negligible impact on the normalized bulk scattering matrix elements except for $\widetilde{\langle S_{34} \rangle}$ [26]. The wavelength of the incident light was 532 nm in the experiments conducted by [26], and the corresponding refractive index of soot was reported as $m = 1.73 + 0.6i$ with the ranges $[1.5, 2.0]$ and $[0.4, 1.1]$ for the real and imaginary parts, respectively. Aggregate representations based on both monodisperse and polydisperse primary particles are generated to investigate the effects of the necking models on the deviations of predicted scattering matrix elements from the measurement data. The real and imaginary parts of the refractive index were changed in the specified ranges

for the monodisperse case to investigate the effect of refractive index on the scattering matrix elements. The effect of refractive index on the scattering matrix elements was found to be insignificant relative to that of necking. Therefore, the results are presented only for $m = 1.73 + 0.6i$. Necking is implemented via LFM and MCCM through a set of necking coefficients identifying the degree of necking between neighbouring primary particles. By definition, the necking coefficient, C_{neck}, is between the interval $[0, 1]$, where the lower and upper bounds correspond to no-neck and full-neck cases, respectively. The cases for which the numerical aggregate models are generated are summarized in Table 3.2. Note that multiple fractal-like aggregates are generated for each case to represent the primary particle size distribution given in [26] and to have adequate realizations of soot aggregates.

Table 3.1: Morphological parameters derived from TEM images for toluene soot aggregates [26].

Soot Sample	$d_{p,g}(nm)$	$\sigma_{p,g}$	$\bar{d}_p(nm)$	k_f	D_f
Toluene	39.57	1.26	40.56	$2.62 - 3.41$	$2.16 - 2.23$

Table 3.2: Specified cases used to generate aggregate representations with necking for the preliminary study on the analysis of different necking models.

Cases	Size Distribution	Necking Model	C_{neck}				
1	Monodisperse	No Neck	0				
2-6		MCCM	0.2	0.4	0.6	0.8	1.0
7-11		LFM	0.2	0.4	0.6	0.8	1.0
12	Polydisperse	No Neck	0				
13-17		MCCM	0.2	0.4	0.6	0.8	1.0
18-22		LFM	0.2	0.4	0.6	0.8	1.0

3.2. Effects of Necking and Polydispersity in Aggregate and Primary Particle Size on the Scattering Matrix

This study focuses on the impacts of necking and polydispersity in aggregate and primary particle size on the scattering matrix elements, S and S^{au}. The information on the accuracy of different necking models in representing necking in soot aggregates provided by the preliminary study (Section 3.1) is utilized in implementation of necking.

In the literature, polydispersity in aggregate and primary particle size are usually represented via log-normal distribution functions defined as

$$p(x) = \frac{1}{ln\sigma_g\sqrt{2\pi}x} exp\left[-\frac{1}{2}\left(\frac{lnx - ln\mu_g}{ln\sigma_g}\right)^2\right] \tag{3.1}$$

where $p(x)$ denotes the probability distribution for the random variable x, μ_g and σ_g are the geometric mean and standard deviation associated with the distribution. The geometric mean and standard deviations representing the aggregate and primary particle size polydispersity of real soot samples are derived from experimental studies in the literature [8,9,26,49,50]. The aggregate and primary particle size distributions are defined over the number of particles in the aggregate (N_p) and primary particle diameter (d_p), respectively. Based on the observations of different aggregate size distributions, μ_{g,N_p} and σ_{g,N_p} are selected as 23.2 and 4.15 [8], which are typical values for flame-soot aggregates [8, 9]. Besides, the impact of aggregate polydispersity on the scattering properties can be clearly observed since relatively large value of σ_{g,N_p} enhances the effect of size distribution. Primary particle polydispersity is defined by $\mu_{g,d_p} = 30.92$ nm and $\sigma_{g,d_p} = 1.36$, corresponding to n-heptane flame-soot aggregates [26]. The selected geometric mean of the primary particle size distribution is a typical value for flame-soot [8, 14, 49]. Similar to the aggregate size distribution, relatively large value of σ_{g,d_p} increases the impact of monomer size distribution on the optical properties. Accordingly, comprehensive information on the potential impact of primary particle polydispersity is provided. Similar to the parameters identifying the size distribution of primary particles provided in Section 3.1, these distributions include the surface

growth of soot particles arising in the process of soot formation and sampling. In addition, the corresponding monodisperse aggregate and primary particle size distributions need to be defined to present the relative impact of polydispersity in aggregate and primary particle size. These definitions are based on the arithmetic mean values of N_p and d_p (denoted as $\overline{N_p}$ and $\overline{d_p}$), which are derived from the specified size distributions as 51 and 32.4 nm, respectively. $\overline{N_p}$ is derived from the specified aggregate size distribution over the interval $[1, 518]$, corresponding to $p(N_p) \geq 5 \times 10^{-5}$. $\overline{d_p}$ is derived from the corresponding primary particle size distribution over the interval $[8, 99]$ nm, corresponding to $p(d_p) \geq 1 \times 10^{-5}$. In addition to the arithmetic mean diameter, the volume mean diameter is also used to generate aggregates formed by monodisperse primary particles. Although the volume mean diameter based approach is used in the literature [6, 22] to account for the impact of primary particle polydispersity, the resultant S^{au} profiles differed more from those of the polydisperse primary particle case. Therefore, only the results associated with the arithmetic mean diameter based approach are presented for the cases of monodisperse primary particle size. The size distributions defined based on the corresponding choice of μ_g and σ_g are shown in Figure 3.1.

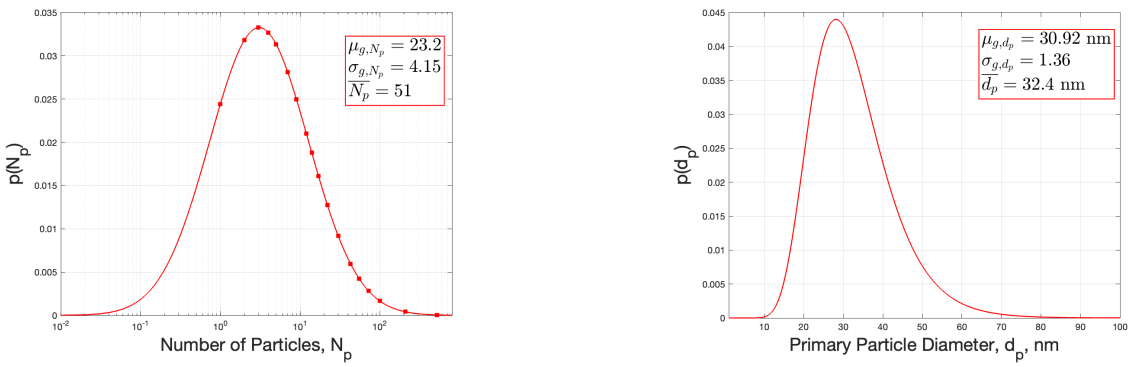

(a) (b)

Figure 3.1: Log-normal distributions defined by the corresponding geometric mean and standard deviations to represent the (a) aggregate size and (b) primary particle size distribution.

The aggregate size distribution is discretized into a number of sample N_p points to calculate the corresponding bulk scattering matrix elements. A convergence study on the number of sample N_p points showed that calculation of the bulk scattering properties over 18 points yield fairly accurate estimations. The selected points are non-uniformly discretized in the interval $[1, 518]$, and shown in Figure 3.1a with square markers. Note that the horizontal axis is provided in the log-scale in Figure 3.1a, and N_p must be an integer to generate aggregate representations.

Table 3.3: Parameter specifications for the cases to be investigated to analyze the effects of necking and polydispersity in aggregate and monomer size.

Cases	Aggregate Size Distribution		Primary Particle Size Distribution		Necking	
	μ_{g,N_p}	σ_{g,N_p}	$\mu_{g,d_p}(nm)$	σ_{g,d_p}	Model	C_{neck}
1	51	1.0	32.4	1.0	-	0.0
2	51	1.0	32.4	1.0	MCCM	0.6
3	51	1.0	32.4	1.0	MCCM	0.8
4	51	1.0	32.4	1.0	MCCM	1.0
5	51	1.0	32.4	1.0	LFM	1.0
6	51	1.0	30.92	1.36	-	0.0
7	23.2	4.15	32.4	1.0	-	0.0
8	23.2	4.15	30.92	1.36	-	0.0

The fractal parameters D_f and k_f are considered as 1.82 and 1.27, respectively. These are typical values for soot aggregates that were shown to yield consistent results obtained from the statistical scaling law and light scattering profile [51]. Necking is implemented via distinct necking coefficients, C_{neck}, quantifying the level of necking between neighbouring primary particles in the aggregate. The modified cylindrical connector model (MCCM) with C_{neck} =0.6, 0.8, 1.0; and the level-set function model [14] with $C_{neck} = 1.0$ are used to model necking. The wavelength of the incident light is set to be 532 nm, which is a typical value used in light scattering experiments. The refractive index of soot is considered as $1.73 + 0.6i$ [26], which was calculated from the wavelength dependent refractive index formulations of soot [52] for 532 nm. Parameter specifications for the cases considered in this study are summarized in Table 3.3.

4. METHODS

The methods followed for the solution of the problems described in Section 3.1 and 3.2 are provided in Section 4.1 and 4.2, respectively.

4.1. Quantitative Analysis of Different Necking Models in Predicting the Scattering Matrix

The main steps of the methodology followed for the quantitative analysis of different necking models in predicting the scattering matrix of soot aggregates are aggregate generation, implementation of necking, scattering simulations, post-processing, and quantitative performance evaluation.

4.1.1. Aggregate Generation

The choice of aggregate representation algorithm is crucial since it affects both the computational time and fidelity of the analysis of necking models in representing the real structure of soot. The accuracy of the chosen aggregate representation algorithm might be evaluated through a comparison of the morphological structure of the resultant aggregates with electron microscopy images associated with soot samples.

Fractal-like Aggregate Generation Environment (FLAGE) by Skorupski et al. [40] is used to generate the aggregate representations for the numerical modeling of scattering. FLAGE is a fast and accurate fractal representation tool developed in Java and it includes various fractal generation algorithms such as DLA, RLA, ballistic aggregation, and modified Filippov's algorithm for both PCA and CCA to generate aggregates formed by both monodisperse and polydisperse primary particles. PCA with DLA algorithm is used in this study for aggregate representation as in [26]. The alternative tunable fractal representation algorithms such as Filippov's algorithm and FracVAL were tested as well. However, they could not converge to an aggregate representation

with the given TEM-derived fractal parameters of $D_f = 2.16$ and $k_f = 2.62$ within a feasible time. Therefore, all aggregate models were generated with FLAGE based on PCA using DLA algorithm (FLAGE-DLA), which yielded approximately the same MSTM results reported by [26] for the monodisperse case.

Aggregate representations with the same morphological parameters and distinct sizes are generated according to the size distribution provided in [26]. J. Liu et al. [26] converted the mobility diameters, d_{mob}, to volume equivalent diameters, d_{ve}, using various conversion factors according to

$$d_{mob} = C \cdot d_{ve} \tag{4.1}$$

where $C = \chi R$ is the conversion factor, χ is the dynamic shape factor of soot, and R is the ratio of Cunningham slip correction factor of d_{mob} to that of d_{ve}.

Four variable (Var1, Var2, Var3, Var4) and six constant conversion factors (1.6, 1.8, 2.0, 2.4, 2.5, 3.0) were considered in [26]. Correlation between χ and d_{mob} was approximated via spline interpolation based on combination of measurements for different soot samples from the literature. The variable conversion factors were based on the spline interpolation for χ and four different constant values of R. Var1 was defined as the product of variable χ and $R = 0.6$. Small conversion factors (Var1 and 1.6) were shown to have relatively good performance in representing the experimental data as compared to the other alternatives [26]. In this study, Var1 provided in [26] is used to convert d_{mob} to d_{ve}. The converted d_{ve} values are then substituted in

$$N_p = \left(\frac{d_{ve}}{\bar{d}_p} \right)^3 \tag{4.2}$$

to determine the number of particles, N_p, with the corresponding number fractions in the aggregate size distribution.

Note that the values of N_p are rounded since the number of particles must be an integer. Aggregate samples with different N_p values are then generated via FLAGE-DLA. Specifications of the sampling of N_p will be discussed in more detail in Section 4.1.4.1. The following step is to implement necking to the generated aggregate representations.

4.1.2. Implementation of Necking

Necking is implemented via a necking coefficient using two different models: *Modified Cylindrical Connector Model* and *Level-set Function Model*.

4.1.2.1. Modified Cylindrical Connector Model. In the definition of the cylindrical connector model provided in [23, 25], the aggregates were assumed to be composed of monodisperse primary particles. In this study, the original cylindrical connector model is modified to represent necking in aggregates of polydisperse primary particles as well, preserving the cylindrical geometry of connectors between adjacent primary particles in soot aggregates. In MCCM, the necks are modeled as a cylinder with radius defined as

$$r_{con} = C_{neck} \cdot min(r_{pi}, r_{pj}) \tag{4.3}$$

where r_{con} is the radius of the cylindrical connector, C_{neck} is the necking coefficient, r_{p1} and r_{p2} are the radii of the i^{th} and j^{th} primary particles, which are in point-touch.

Therefore, neck formation occurs between pairs of particles that are in point-touch only for MCCM by definition. MCCM is fast and easy to implement. Based on its performance in representing the real structures, it might serve as an alternative simple model to represent necking in polydisperse aggregates. In Figure 4.1, necking is implemented via MCCM with different coefficients to a cluster of three particles with equal (a, b, c) and unequal radii (d, e, f), and the resultant structures are illustrated through a large number of evenly spaced discrete points.

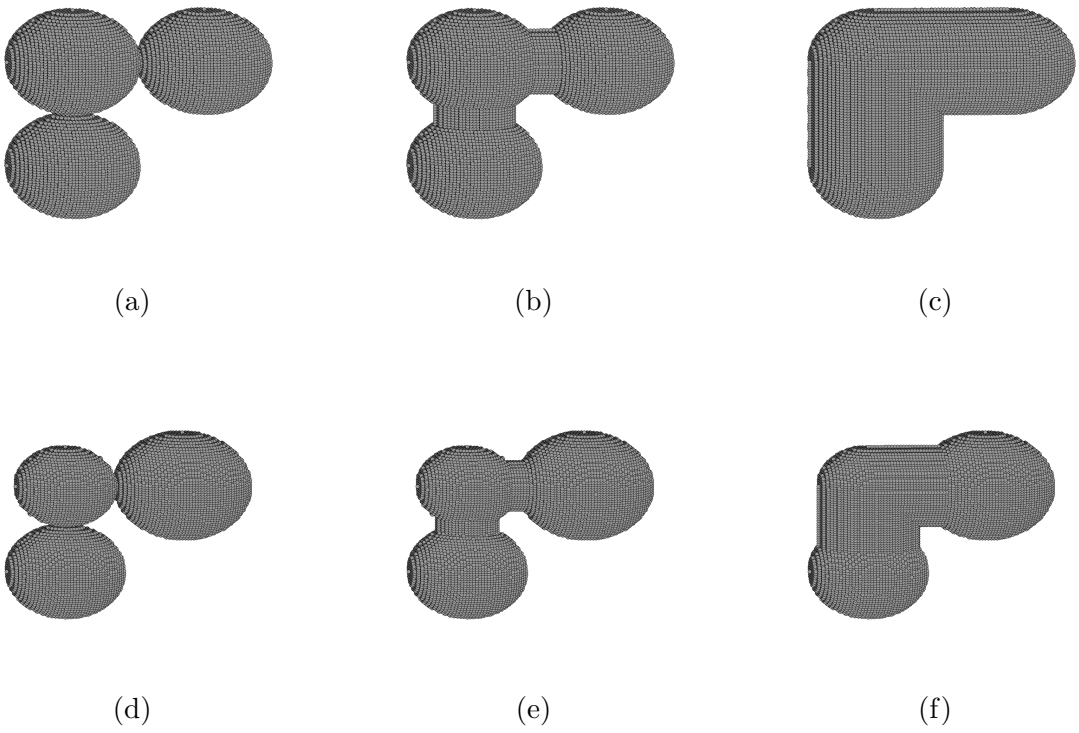

(a) (b) (c)

(d) (e) (f)

Figure 4.1: Necking implemented via MCCM to a cluster of three particles with (a) equal radii for $C_{neck} = 0.2$, (b) equal radii for $C_{neck} = 0.6$, (c) equal radii for $C_{neck} = 1.0$, (d) unequal radii for $C_{neck} = 0.2$, (e) unequal radii for $C_{neck} = 0.6$, and (f) unequal radii for $C_{neck} = 1.0$.

4.1.2.2. Level-set Function Model. In this model, necking is represented via a 3D level-set function defined as

$$\psi(x,y,z) = \sum_{i=1}^{N_p} \frac{1}{2} \cdot \left(1 + erf\left(-\frac{1}{C_{neck}}\left(\frac{l_i}{r_{pi}} - 1\right)\right)\right) \tag{4.4}$$

where ψ is a scalar identifying whether the point (x, y, z) lies within the aggregate or not, l_i is the distance of the point (x, y, z) from the center of the i^{th} primary particle, and r_{pi} is the radius of the i^{th} primary particle [14]. The point (x, y, z) is said to be inside the aggregate if $\psi > 0.5$. Figure 4.2 shows implementation of necking to the same clusters of particles given in Figure 4.1 via LFM with different coefficients. The resultant structures are represented by a large number of evenly spaced discrete points.

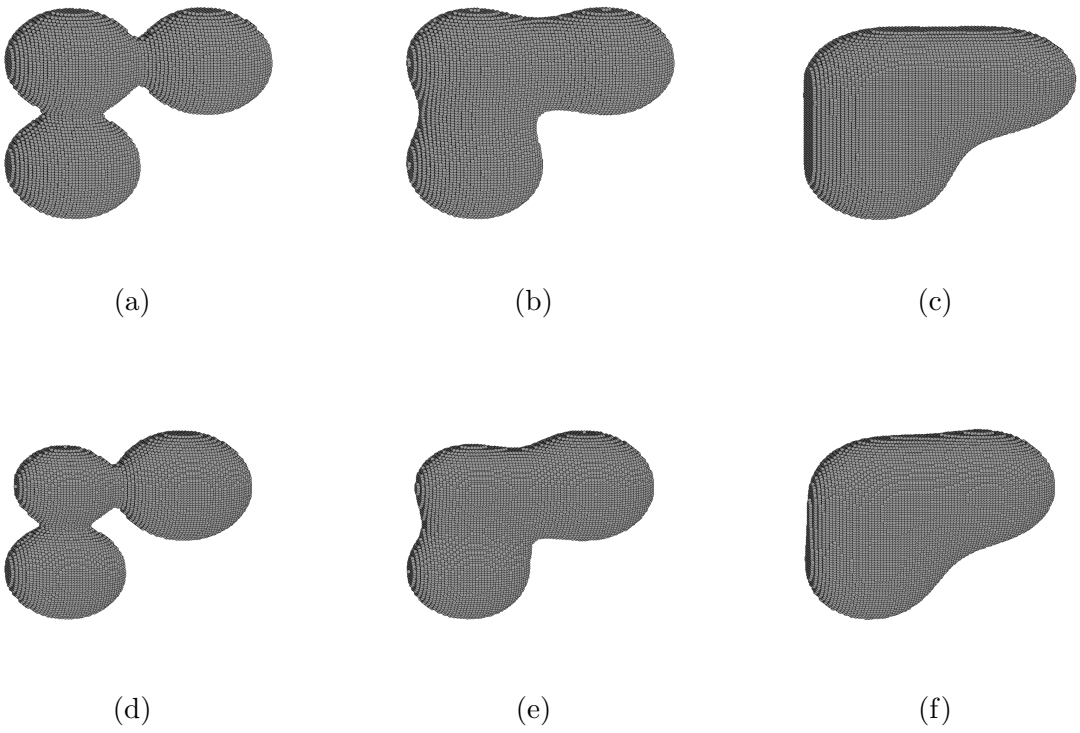

Figure 4.2: Necking implemented via LFM to a cluster of three particles particles with (a) equal radii for $C_{neck} = 0.2$, (b) equal radii for $C_{neck} = 0.6$, (c) equal radii for $C_{neck} = 1.0$, (d) unequal radii for $C_{neck} = 0.2$, (e) unequal radii for $C_{neck} = 0.6$, and (f) unequal radii for $C_{neck} = 1.0$.

Note that by definition of the level-set function, the neck formation occurs between *neighbouring* primary particles, meaning that necking material might be added in between particles that are near to each other but not in point-touch as necking coefficient increases. Moreover, new points that are slightly outside of the particle surfaces begin to be included in the aggregate as necking coefficient becomes closer to 1. Therefore, LFM adds more volume to the aggregate with increasing necking coefficient as compared to the MCCM.

4.1.3. Scattering Simulations

Scattering simulations are conducted for verification of the aggregate representations through a comparison with the simulation results of [26]. Third version of the multi-sphere T-matrix (MSTM) code developed by Mackowski and Mishchenko [16], MSTM v3.0, was used in the work of J. Liu et al. [26].

Then the scattering matrix elements of the aggregates with necking implemented through different models and levels are estimated, also considering the limiting case of compactness to understand the morphology of the real aggregates and the trend with necking. Scattering simulations for the aggregates with necking are conducted using the discrete dipole approximation code, DDSCAT, by Draine and Flatau [17] which allows to conduct scattering simulations of arbitrarily shaped particles. The results are averaged over 500 orientations, and the spacing between dipoles is set to be 5 nm, which yields dipole per wavelength (dpl) greater than 100. This specified dipole spacing satisfies the conservative applicability criterion for DDA [43], which is defined as

$$|m|kd < 0.5 \tag{4.5}$$

where m is the complex refractive index of the particle material, $k = \frac{2\pi}{\lambda}$ is the wavenumber, and d is the dipole spacing.

Furthermore, a grid independence study was conducted on the dipole spacing, and it was observed that reducing the dipole distance below 5 nm does not change the resultant scattering matrix element profiles considerably. Variance in the calculated scattering matrix elements of the aggregate representations created by FLAGE-DLA is expected due to the randomization in fractal generation process. The effect of randomization might be diminished by averaging the resultant scattering matrix elements over a number of aggregate representations generated for the same set of morphological parameters. For the monodisperse cases, the scattering simulations are conducted for a single aggregate representation for each aggregate with distinct d_{ve} since the effect

of randomization in fractal generation was studied and observed to be negligible for these cases. On the other hand, for the polydisperse cases, the scattering simulations are conducted for 10 distinct aggregate representations generated via FLAGE-DLA for each aggregate with specific d_{ve}, considering that the magnitude of fluctuations in the scattering matrix of different polydisperse aggregates might be significant.

Finally, Mie theory is implemented via the MATLAB code developed by Mätzler [53] to calculate the scattering matrix elements associated with the spheres with equivalent d_{ve} to that of distinct aggregate samples. In this manner, the scattering matrix elements are calculated analytically for the limiting case of compactness for each distinct aggregate sample, which might give information about the compactness of the real aggregate samples and the interconnection between introducing necking and aggregate morphology.

4.1.4. Post-processing

The methodologies in regards to post-processing of scattering simulation results and measurement data are explained in Sections 4.1.4.1 and 4.1.4.2, respectively.

4.1.4.1. Simulation Results. The experimental data provided in [26] are normalized bulk data obtained from a large number of samples over a short duration of time. The bulk scattering matrix elements are calculated numerically through integration of scattering matrix elements over the aggregate representations generated via FLAGE-DLA with different d_{ve} based on the distribution provided in [26]. As in [26], the integration is conducted as

$$\left\langle S_{ij}^{au}\left(\theta\right)\right\rangle = \frac{\int_{d_{ve,min}}^{d_{ve,max}} S_{ij}^{au}\left(\theta, d_{ve}\right) C_{sca}\left(d_{ve}\right) n\left(d_{ve}\right)\, dd_{ve}}{\int_{d_{ve,min}}^{d_{ve,max}} C_{sca}\left(d_{ve}\right) n\left(d_{ve}\right)\, dd_{ve}}. \tag{4.6}$$

The integration is calculated numerically via the simple Trapezoidal rule using the scattering matrix elements, corresponding scattering cross-sections, and number fractions for distinct aggregates with specific d_{ve}. J. Liu et al. [26] suggested to consider aggregates with d_{ve} from 30 nm to 460 nm with 10 nm increment, which covers almost the entire aggregate size distributions for toluene and n-heptane soot samples.

However, there are some limitations on the sampled d_{ve} points associated with the aggregate representation tool, FLAGE, the computation time for dipole generation and scattering simulations considering implementation of necking. FLAGE-DLA allows representation of aggregates with $N_p \geq 5$ which limits the minimum allowable d_{ve} to approximately 70 nm. Furthermore, the number of distinct aggregate samples to be used in the integration might be reduced to decrease the computational load considering the number fraction associated with specific samples and the resultant bulk scattering matrix elements. The bulk scattering matrix elements were calculated for various d_{ve} samplings and compared. The differences between the bulk scattering matrix elements were not significant. Accordingly, the sample d_{ve} points to be used in this study were chosen from 160 nm to 400 nm with 30 nm increment.

After the number of primary particles, N_p, associated with the specified d_{ve} was calculated via Equation (4.2) and the corresponding aggregates were generated by FLAGE-DLA, necking is implemented to the aggregate representations through different necking models and coefficients as defined in Table 3.2. Then, scattering simulations are conducted for each of these aggregates via DDSCAT to obtain S_{ij}^{au} and C_{sca}, which are integrated to obtain the bulk scattering matrix elements according to Equation (4.6). The bulk scattering matrix elements are then normalized as

$$\widetilde{\langle S_{ij}(\theta)\rangle} = \begin{cases} \dfrac{\left\langle S_{ij}^{au}(\theta)\right\rangle}{\left\langle S_{ij}^{au}(10^{\circ})\right\rangle} & i=j=1 \\ -\dfrac{\left\langle S_{ij}^{au}(\theta)\right\rangle}{\left\langle S_{11}^{au}(\theta)\right\rangle} & i=1, j=2 \\ \dfrac{\left\langle S_{ij}^{au}(\theta)\right\rangle}{\left\langle S_{11}^{au}(\theta)\right\rangle} & otherwise \end{cases} \tag{4.7}$$

which are then compared with the measured normalized bulk scattering matrix elements provided in [26].

4.1.4.2. Measurement Data. The measurement data are subjected to post-processing to derive the experimental bulk scattering matrix elements to provide further information on the morphology of both the real toluene soot samples and the aggregate representations with necking since normalization reduces the morphological information that would be obtained from distinct scattering matrix elements. Therefore, considering both normalized and bulk scattering measurement data might provide more information on morphology.

Using the two definitions of the scattering matrix, the equation relating the experimental $\langle\widetilde{S_{11}(\theta)}\rangle$ with $\langle S_{11}^{au}(10^{\circ})\rangle$ is derived as

$$\frac{1}{2}\int_{0}^{\pi}\langle\widetilde{S_{11,exp}(\theta)}\rangle sin\theta\, d\theta = \frac{1}{\left\langle S_{11,exp}^{au}(10^{\circ})\right\rangle} \tag{4.8}$$

where $\left\langle S_{11,exp}^{au}(10^{\circ})\right\rangle$ is to be determined using the measured $\langle\widetilde{S_{11}(\theta)}\rangle$ [54]. Then, $\left\langle S_{ij}^{au}(\theta)\right\rangle$ are calculated by substituting $\left\langle S_{11,exp}^{au}(10^{\circ})\right\rangle$ into (4.7).

4.1.5. Quantitative Performance Evaluation

The quantitative analysis of performance of different necking models in predicting the measured scattering matrix elements are based on a predefined error metric. In addition, certain evaluation metrics are suggested based on the physical meanings of different scattering matrix elements and their combinations. Detailed explanation in regards to the error definition and suggested evaluation metrics are provided in Sections 4.1.5.1 and 4.1.5.2, respectively.

4.1.5.1. Error Definition. The performances of different necking models and necking coefficients are analyzed based on normalized root-mean-square error (NRMSE), for both the normalized and bulk scattering matrix element data, which is defined as

$$NRMSE_{k,m}^{S_{ij}} = \sqrt{\frac{1}{N_\theta}\sum_{n=1}^{N_\theta}\left[\frac{\left(\mu_{S_{ij,exp}(\theta_n)} - \overline{S_{ij,km}\left(\theta_n\right)}\right)}{3\cdot\sigma_{S_{ij,exp}(\theta_n)}}\right]^2} \tag{4.9}$$

where subscripts k and m denote necking model and necking coefficient respectively, N_θ is the number of discrete scattering angles for which the experimental data are measured, μ denotes the mean experimental normalized or bulk S_{ij} obtained over a large number of measurements conducted in about 1 s and σ is the corresponding standard deviation. Here, the overline indicates the average value of normalized or bulk $S_{ij,km}$, which is obtained by generating distinct aggregate representations for each d_{ve}, integrating over the aggregate size distribution using these sets of alternative aggregates separately, and then taking the average.

As can be seen in Equation (4.9), $NRMSE$ is defined based on the normalization of mean absolute error in $S_{ij,km}$ at distinct scattering angles obtained from scattering simulations by the maximum error in the measurement data at the corresponding scattering angle defined by $3\sigma_{S_{ij,exp}(\theta)}$. It might also be informative to introduce different error definitions such as relative errors in $S_{ij,km}$ profile. However, relying on relative errors might be misleading considering that it might amplify the effect of negligible local deviations in the scattering matrix elements where the magnitudes of the deviations are relatively small with respect to measurement uncertainty. Therefore, relative errors in the scattering matrix elements are not introduced to the error metric definition in this study.

4.1.5.2. Evaluation Metrics. Even though the NRMSE values corresponding to the overall bulk and normalized scattering matrix elements reflect comprehensive information on the morphology of the aggregates, the information specific to necking might be obscured considering the physical meanings of different scattering matrix elements.

Moreover, measurement of all scattering matrix elements requires more complex experimental setups, and such data might be limited. As it is important to outline a methodology for evaluating proper necking model for soot utilizing from simpler apparatus, identifying more critical scattering matrix elements is required. Therefore, three different combinations of NRMSE associated with various normalized and bulk scattering matrix elements are suggested for analyzing the performance of different necking models considering the physical meanings of the normalized and bulk scattering matrix elements.

(i) $\langle S_{11}^{au} \rangle$, $\langle S_{12}^{au} \rangle$, and $\widetilde{\langle S_{12} \rangle}$

- This combination is known to be related to certain morphological parameters of the aggregates such as size and compactness of the aggregate, primary particle size distribution, and linear polarization ratio which might provide useful information for characterization of necking in the aggregates.
- $\widetilde{\langle S_{11} \rangle}$ is not used since the bulk data would be more informative about the distribution of the scattered light.
- Measurements of these quantities might be conducted with less complex experimental apparatus.

(ii) $\langle S_{11}^{au} \rangle$, $\langle S_{22}^{au} \rangle$, and $\widetilde{\langle S_{22} \rangle}$

- Considering that this alternative combination has the parameters associated with morphological characteristics such as size and compactness of the aggregate, shape of the particles, and depolarization ratio, it might be utilized in the analysis of the proper necking model.
- This combination is promising since it involves parameters that are sensitive to the morphology of the particles and not affected by the change in the aggregate size/volume as opposed to the general trend with other normalized or bulk scattering matrix elements.
- Measurements of these quantities might be conducted with less complex experimental apparatus.

(iii) $\langle S_{11}^{au} \rangle$, $\langle S_{12}^{au} \rangle$, $\langle S_{22}^{au} \rangle$, $\widetilde{\langle S_{12}^{au} \rangle}$, and $\widetilde{\langle S_{22} \rangle}$

- This combination includes all the elements of the 1^{st} and 2^{nd} combinations.
- It might be useful in the case when implementation of necking occurred to be not satisfactory in terms of reducing the deviations of the simulation results from the measurement data for certain elements utilized in the 1^{st} and 2^{nd} combinations.

4.2. Effects of Necking and Polydispersity in Aggregate and Primary Particle Size on the Scattering Matrix

The main steps of the methodology followed for investigation of the effects of necking and polydispersity in aggregate and primary particle size on the scattering matrix of soot are aggregate generation, implementation of necking, scattering simulations, and post-processing.

4.2.1. Aggregate Generation

Aggregates are generated via FracVAL by Moran et al. [41], based on the morphological parameters specified for the cases provided in Table 3.3. FracVAL was shown to have adequate performance in preserving the prescribed fractal parameters for individual aggregates as well as an ensemble of aggregates [41]. Contrary to the problem described in Section 3.1, convergence problem associated with FracVAL does not occur in this problem since the specified set of fractal parameters is not extreme.

The aggregate size distribution is discretized into a number of sample N_p points to calculate the corresponding bulk scattering matrix elements. A convergence study on the number of sample N_p points showed that calculation of the bulk scattering properties over 18 points yield fairly accurate estimations. The selected points are non-uniformly discretized in the interval $[1, 518]$. Calculation of the bulk scattering matrix elements for the ensemble of aggregates with non-uniform size distribution is explained in Section 4.2.4.

The resultant scattering matrix elements are subject to uncertainty that leads to fluctuations due to random nature of fractal generation algorithm. Therefore, multiple aggregate representations are generated for aggregates with a specific N_p, and averaged scattering matrix elements are presented to reduce the magnitude of the fluctuations. The number of different aggregate representations generated for distinct N_p are specified as 10 and 30 for monodisperse and polydisperse primary particle size distributions, respectively.

4.2.2. Implementation of Necking

Two different necking models, MCCM and LFM, are used to represent necking in the generated aggregate representations with different necking coefficients as defined in Table 3.3 (Cases 2-5). LFM is used to present the limiting effect of necking on the scattering behavior as it results in larger aggregate volume variation relative to the alternative models as discussed in Section 4.1.2.2. Formulations for these models are provided in Sections 4.1.2.1 and 4.1.2.2.

Additionally, two different approaches are utilized in implementation of necking. The first approach is the *Constant Monomer Radius Approach*. In this approach, the primary particle radii associated with the fractal representations generated via FracVAL are kept constant during implementation of necking. Correspondingly, the effect of aggregate volume variation is included in the resultant scattering matrix elements. The other approach, *Constant Aggregate Volume Approach*, is based on decreasing primary particle diameters such that the resultant aggregate volume remains unchanged after implementation of necking. Accordingly, the effect of aggregate volume variation due to implementation of necking can be identified. The accuracy of representing the effect of necking on the optical behavior based on the resultant aggregate volume variation, as proposed by Teng et al. [25], is evaluated with this approach.

4.2.3. Scattering Simulations

Scattering properties of the aggregate representations with no necking (Cases 1, 6, 7, and 8) are calculated by MSTM using the software, MSTM v3.0, developed by Mackowski and Mishchenko [16]. Whereas, scattering properties of the aggregates including necking (Cases 2-5) are approximated by DDA using the software, DDSCAT, developed by Draine and Flatau [17].

The accuracy of approximations obtained from DDSCAT is dependent on the number of target orientations to calculate orientation-averaged properties, and the number of dipoles that are used to represent the target structure. The number of target orientations is specified as 500, which was observed to yield converged orientation averaged solutions for the scattering properties. The dipole separation distance, d, is set to be 2 nm corresponding to a dipole per wavelength (dpl) ratio larger than 250. Refinement study on d, and comparison via MSTM results for no necking case justified the specified value of d for producing sufficiently accurate results.

4.2.4. Post-processing

The scattering simulation results are subjected to post-processing to obtain the approximate scattering properties associated with the cases specified in Table 3.3. For the cases of polydisperse aggregate size distribution (Cases 7 and 8), the bulk scattering properties are obtained by integration over an ensemble of aggregates with different N_p. The formulation for calculation of S^{au} is similar to Equation (4.6). The difference is that the integrations are conducted over N_p instead of d_{ve}, and the log-normal probability function (p) is used instead of the number fraction (n). The formulation used to calculate the elements of S for Cases 7 and 8 is similar to that utilized in calculating the elements of S^{au}. The only difference is that the integration is conducted over $S_{ij}(\theta, N_p)$, and $C_{sca}(N_p)$ is not present in the integrals accordingly.

The scattering matrix elements for all cases are presented through the corresponding 95% confidence intervals for their mean values over the specified number of different aggregate representations. Student's t-distribution is used to obtain more reliable statistics, since the sample sizes for aggregates formed by both monodisperse and polydisperse primary particles are small.

In addition, the radius of gyration (R_g) and the asymmetry factor (g) for the specified cases are calculated to investigate the relation between R_g and S^{au} profiles quantitatively. Yon et al. [24] showed that the impacts of necking and overlapping on the asymmetry factor seem to be related with their effects on the radius of gyration. The asymmetry factor is calculated over the scattering phase function, S_{11}^{au}, as

$$g = \frac{1}{4} \int_0^{\pi} S_{11}^{au}(\theta)\, sin(2\theta)\, d\theta. \tag{4.10}$$

where θ is the scattering angle [55].

The radius of gyration of an individual aggregate representation is calculated as

$$R_g = \sqrt{\frac{1}{m_{agg}} \sum_{i=1}^{N_p} m_{pi} \left({R_i}^2 + {r_{gi}}^2 \right)} \tag{4.11}$$

where m_{agg} and m_{pi} are the mass of the aggregate and the i^{th} primary particle, R_i is the distance of the center of the i^{th} primary particle from the center of mass of the aggregate, and r_{gi} is the radius of gyration of the i^{th} primary particle [42]. Note that $r_{gi} = \sqrt{(3/5)\, {r_{pi}}^2}$ where r_{pi} is the radius of the i^{th} primary particle.

5. RESULTS & DISCUSSIONS

The problems described in Sections 3.1 and 3.2 are solved based on the methodologies provided in Sections 4.1 and 4.2, respectively. Corresponding results are presented and discussed in Sections 5.1 and 5.2.

5.1. Quantitative Analysis of Different Necking Models in Predicting the Scattering Matrix

Scattering simulations are conducted for aggregates formed by both monodisperse and polydisperse primary particles. Even though the primary particle size distribution is known to be polydisperse, providing the results for the monodisperse case and demonstrating their consistency with those for the polydisperse case might be of interest and insightful. Furthermore, the number of fractal representations generated for the same set of morphological parameters is greater for the polydisperse case attributed to the randomization in particle size and aggregate morphology. Therefore, in the ideal case, scattering simulations should be conducted over a large number of fractal representations for each set of morphological parameters to ensure the reliability of the results, which will result in excessive computational load. In this study, the number of fractal representations, N_{frac}, is limited to 10 for each sample d_{ve} point for the polydisperse cases to achieve a feasible simulation time. Considering that the sample size might be insufficient to obtain reliable statistics, the results obtained for the monodisperse case might be utilized in assessing the convergence for those of the polydisperse case if the effect of necking on the scattering matrix elements is more pronounced than that of polydispersity. The effects of necking and polydispersity on normalized and bulk scattering matrix elements were compared and the impact of necking was observed to be dominant.

5.1.1. Aggregates Formed by Monodisperse Primary Particles

The results associated with the computed scattering matrix elements for aggregates formed by monodisperse primary particles and evaluation of different necking models based on the predefined error metric, NRMSE, are presented in Sections 5.1.1.1 and 5.1.1.2, respectively.

5.1.1.1. Computed Scattering Matrix Elements. Normalized and bulk scattering matrix element plots for the monodisperse case are provided in Figure 5.1 and Figure 5.2, respectively. As can be seen in Figure 5.1, the effect of necking on the scattering matrix elements is more pronounced when it is implemented via LFM rather than MCCM. This might be attributed to the resultant change in the aggregate size/volume with implementation of necking. Necks are formed not only in between the particles in point-touch, but also the neighbouring particles based on the definition of LFM, which yields greater aggregate volume as compared to that obtained for MCCM. Therefore, the resultant effects of necking implemented via LFM with smaller necking coefficients might exhibit similar behavior with those implemented via MCCM with larger necking coefficients as can be observed in Figure 5.1. Hence, based on the observations on the overall normalized scattering matrix elements for the monodisperse case, it might be concluded that MCCM might be used as an easier alternative of LFM to represent necking unless an excessive amount of necking is present in the real aggregates of interest.

Based on the results shown in Figure 5.1 for different necking models and different necking coefficients, different trends are observed for different elements. The effect of necking is insignificant for $\widetilde{\langle S_{12} \rangle}$, $\widetilde{\langle S_{33} \rangle}$, and $\widetilde{\langle S_{44} \rangle}$; whereas considerable changes are observed for $\widetilde{\langle S_{11} \rangle}$, $\widetilde{\langle S_{22} \rangle}$, and especially $\widetilde{\langle S_{34} \rangle}$. The negligible effects of necking observed for certain normalized scattering matrix elements might be attributed to their physical meanings. $\widetilde{\langle S_{33} \rangle}$ and $\widetilde{\langle S_{44} \rangle}$ profiles are related to the macro-structural properties of the aggregate, which are not considerably affected by necking. Additionally, the loss of morphological information due to normalization of bulk scattering matrix elements

should not be ignored. The resultant effect of necking on specific bulk scattering matrix elements might be diminished by normalization depending on the corresponding $\langle S_{11}^{au} \rangle$ profile. Another observation on the trends with necking for different elements is that the trends for all elements exhibit monotonic behaviors except for that of $\widetilde{\langle S_{34} \rangle}$. For $\widetilde{\langle S_{34} \rangle}$, two opposite trends are observed with increasing necking coefficients. Observations on $\widetilde{\langle S_{34} \rangle}$ profile indicate that there is a critical value of necking coefficient for each necking model after which the trend is reversed. The peak value of $\widetilde{\langle S_{34} \rangle}$ decreases monotonically up to the critical value of necking coefficients, which are around 0.4 and 0.8 for LFM and MCCM, respectively. Increasing the necking coefficients further results in an increase in the peak value of $\widetilde{\langle S_{34} \rangle}$. Considering the sensitivity of S_{34} to the deviations from the Rayleigh regime and the fact that it has too small magnitudes, this phenomenon might be attributed to the changes in the multiple scattering effects associated with the structural modifications in the aggregate due to implementation of necking via different necking coefficients.

Examining the effects of different necking models and coefficients on producing the overall normalized scattering matrix element data shown in Figure 5.1, it can be concluded that introducing necking to the aggregate representations is not sufficient to re-produce the corresponding measurement data. However, an improvement is observed, which might be utilized in characterization of necking in the aggregates. While the deviations of computed $\widetilde{\langle S_{11} \rangle}$ profile from the measurement data are visible mainly at backward scattering angles, considering the log-scale, which amplifies negligible fluctuations at the backward scattering angles, evaluation of the proper necking model based on $\widetilde{\langle S_{11} \rangle}$ profile should be conducted quantitatively via the NRMSE. The improvement in producing the experimental data with implementation of necking is not considerable for $\widetilde{\langle S_{12} \rangle}$. Examining the $\widetilde{\langle S_{22} \rangle}$ profile, introducing necking to the aggregate representations decreases the deviations from the measurement data, but there still exist significant deviations. Therefore, the identification of the proper necking model should not be based on $\widetilde{\langle S_{22} \rangle}$ only. As can be observed in the $\widetilde{\langle S_{33} \rangle}$ and $\widetilde{\langle S_{44} \rangle}$ plots, the deviations at the backward scattering angles are reduced for the aggregates with necking but the effect is too small that the profiles for different necking models

are almost indistinguishable. For the $\widetilde{\langle S_{34} \rangle}$ profile, implementation of necking via LFM with $C_{neck} = 1.0$ seems to perform well in resembling the experimental data. However, this might be misleading since it includes $\langle S_{11}^{au} \rangle$ as well, which might diminish the resultant errors in $\widetilde{\langle S_{34} \rangle}$ for different sets of necking models and coefficients.

Although the plots in Figure 5.1 are informative about the morphology of the real aggregates and the effect of necking on each element, the morphological information is reduced due to normalization of the bulk elements. Therefore, the analysis of the proper necking model associated with the aggregates of interest should not be conducted using the normalized data only as the effect of different necking models for approximating the measurement data might be misleading.

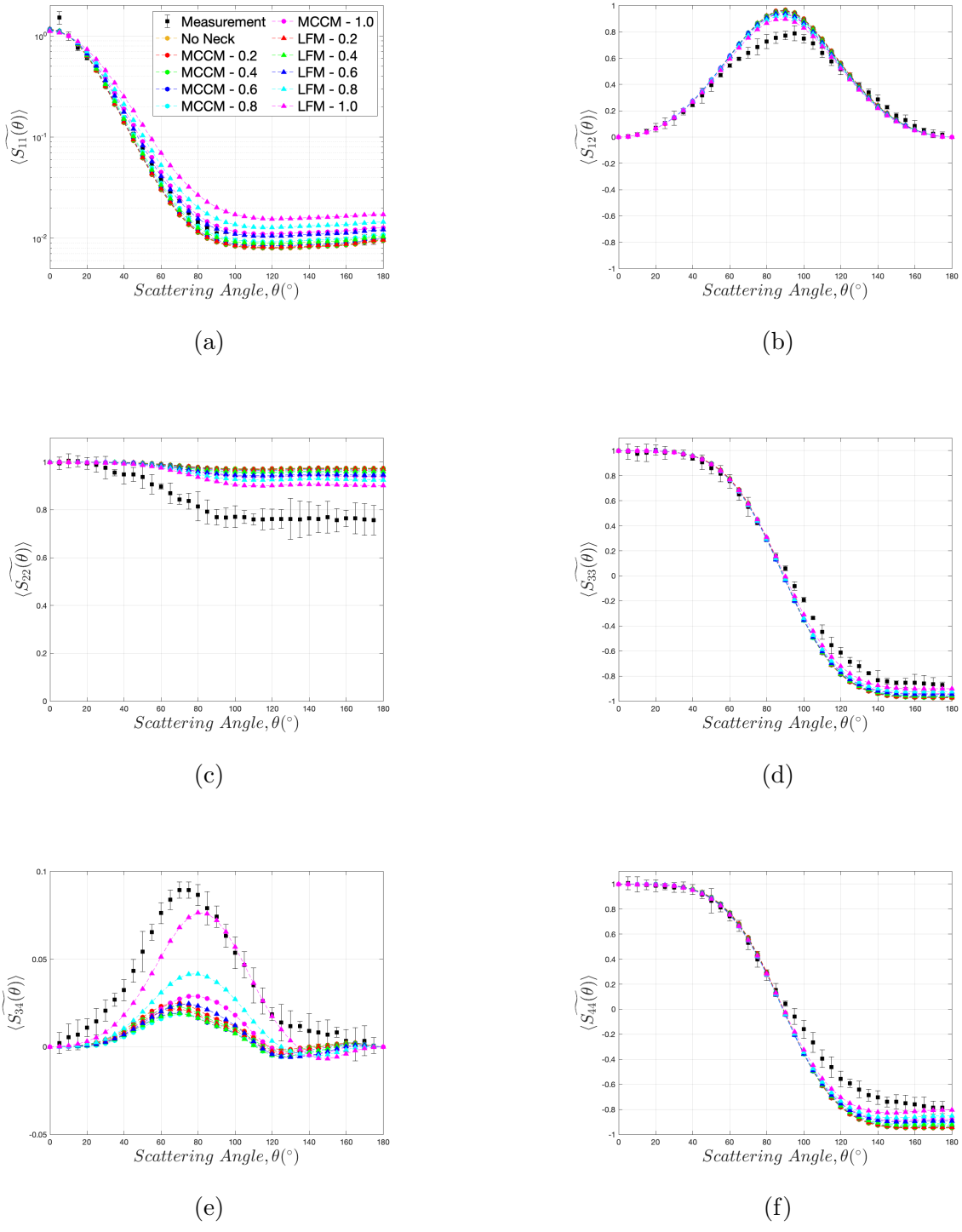

Figure 5.1: Normalized bulk scattering matrix elements obtained from measurement data provided in [26], and DDSCAT simulations for different necking models and coefficients for the monodisperse case.

Figure 5.2 illustrates the bulk scattering matrix elements derived from measured normalized scattering matrix elements [26], DDSCAT simulations conducted over aggregate representations with necking introduced via LFM and MCCM, and Mie theory implemented to the volume equivalent spheres associated with the sample aggregates representing the aggregate size distribution. Comparing the relative effects of necking implemented via LFM and MCCM on the bulk scattering matrix elements shown in Figure 5.2, the effect of necking obtained for LFM is observed to be greater than that for MCCM as in the normalized data, as discussed earlier based on normalized data. Likewise, considering the similarity between the profiles corresponding to LFM with small C_{neck} and MCCM with large C_{neck}, it can be concluded that MCCM can be used as an alternative for LFM when the amount of necking is not extremely large.

Comparing the experimental data, simulation results, and the Mie solution provided in Figure 5.2, it can be observed that the Mie solution deviates further away from the experimental data compared to the simulation results for all bulk scattering matrix elements, except for $\langle S_{34}^{au} \rangle$. In $\langle S_{34}^{au} \rangle$ profile, although the peak value of the measurement data is closer to that of Mie theory, the position of the peak measurement data is further away from that of Mie theory. Considering that the profiles obtained via the Mie theory represent the limiting case of fully compact structure for each aggregate, it might be deduced that the real aggregates on which the light scattering experiments are conducted have more compact structures than the numerically generated aggregate representations. This is consistent with the statement made by J. Liu et al. [26], who indicated that the treatments of soot sampling might enlarge the primary particle sizes, modify the fractal parameters, and result in more compact structures. The effect of implementing necking would be analyzed more adequately if the morphological parameters of soot aggregates used in the light scattering experiments were more accurately determined.

As can be seen from Figure 5.2, the effect of necking on the bulk scattering matrix elements is more pronounced as compared to that on the normalized bulk scattering matrix elements, which is associated with recovering information lost in normalization. The trends in the bulk scattering matrix element plots with implementation of necking corresponding to $\langle S_{11}^{au} \rangle$, $\langle S_{22}^{au} \rangle$, $\langle S_{33}^{au} \rangle$, and $\langle S_{44}^{au} \rangle$ are similar to each other. As the necking coefficient is increased towards the full-neck case, the values of these scattering matrix elements at forward scattering angles decrease; whereas slight increases are observed at backward scattering angles. Considering the trend with necking and the profile obtained via Mie theory, implementing necking with increasing necking coefficient seems to approach the limiting case of full compactness. Furthermore, the effect of necking with increasing necking coefficient is the opposite to that of increasing the particle diameter, d_p, and the number of particles, N_p, which was studied by Manickavasagam and Mengüç [46]. Therefore, introducing necking to the aggregates is directly related to the compactness and structural symmetry of the aggregates, and inversely related to the radius of gyration. In the $\langle S_{12}^{au} \rangle$ profile, shifts in the peak angle towards larger scattering angles are observed when necking is implemented via growing necking coefficient. Therefore, the profiles are approaching those of the Mie theory considering the peak angles, which is consistent with the trend observed in $\langle S_{11}^{au} \rangle$, $\langle S_{22}^{au} \rangle$, $\langle S_{33}^{au} \rangle$, and $\langle S_{44}^{au} \rangle$. As for the $\langle S_{34}^{au} \rangle$ profile, the trend with necking is similar to that observed in Figure 5.1. The critical values of necking coefficients are the same as observed from the normalized data plots. Besides, the peak angle tend to shift towards larger scattering angles when necking is implemented with increasing necking coefficients. Hereby, the profiles approach the limiting case of full compactness as necking is introduced with larger coefficients to the aggregate representations. This is consistent with the trends observed in the other elements. Moreover, similar to $\langle S_{12}^{au} \rangle$, the trend with necking in $\langle S_{34}^{au} \rangle$ is the opposite to that of increasing d_p and N_p, which results in a shift in the peak angle towards smaller scattering angles and eventually multiple extrema [46]. Considering the trends in bulk scattering matrix elements, the effect of necking might be expressed in terms of characteristic parameters of the aggregate such as R_g, d_{ve}, and the fractal parameters. This expression might be utilized to resemble the effect of necking on the scattering matrix elements of the aggregate representations with no

neck. Thus, more efficient methods such as MSTM might be used to conduct scattering simulations, which yield good accuracy at reduced computational time. Further studies are required to identify the interrelation between necking and the characteristic parameters that are significantly affected by implementation of necking.

Introducing necking improves the accuracy of prediction of the overall measurement data, as observed in Figure 5.2, but deviations are still observed. It is not straightforward to determine the proper necking models and coefficients based on observations of the plots considering the magnitudes of standard deviations in the measurements corresponding to different elements at distinct scattering angles, except for $\langle S_{34}^{au} \rangle$. For $\langle S_{34}^{au} \rangle$, LFM with $C_{neck} = 1.0$ seems to exhibit the best performance in resembling the measurement data. However, the analysis should not be based merely on this element considering that it is sensitive to many morphological parameters that might not be utilized in characterization of necking. Therefore, quantitative analyses should be conducted to derive the best necking model that provides the minimum overall deviation from the measurement data.

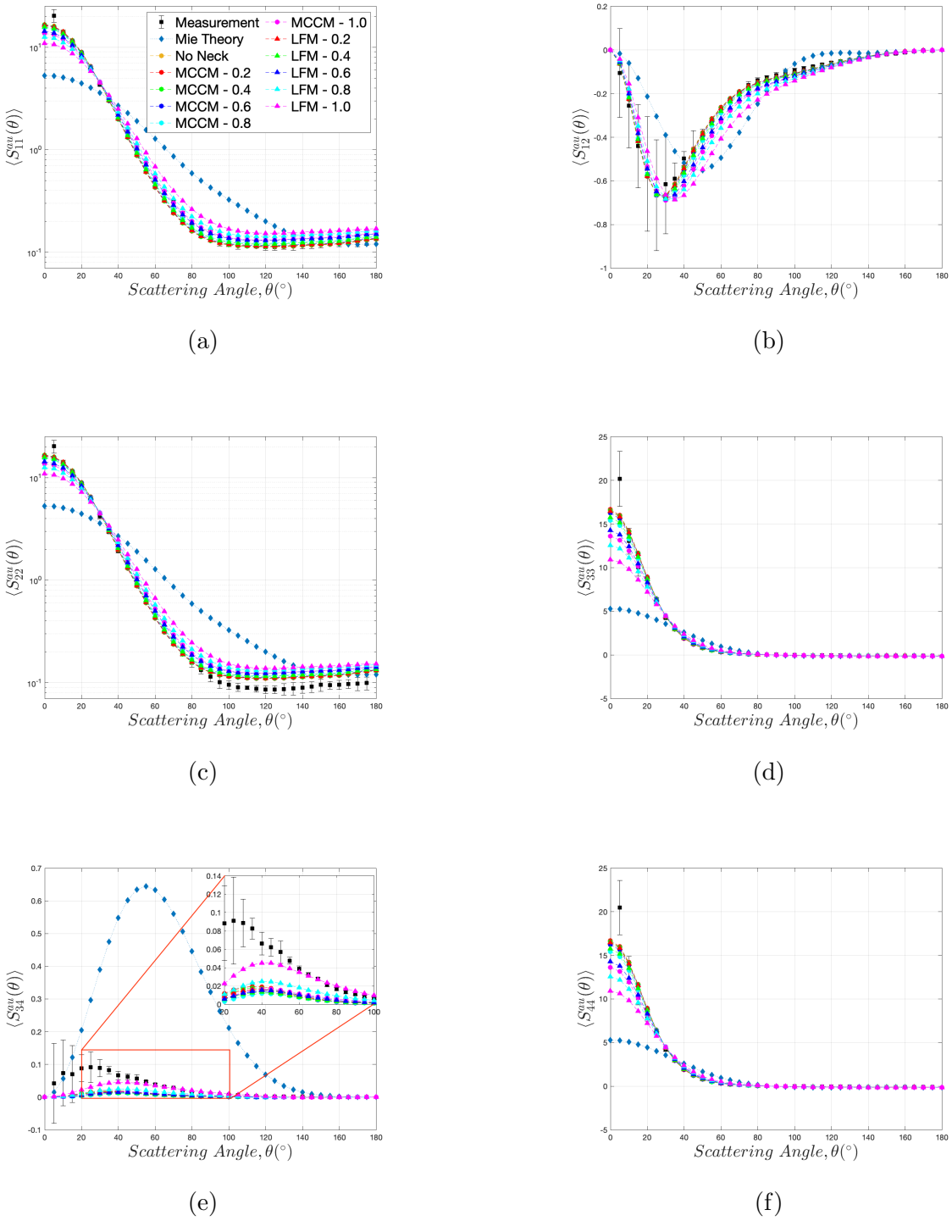

(a) (b) (c) (d) (e) (f)

Figure 5.2: Bulk scattering matrix elements obtained from normalized measurement data provided in [26], and DDSCAT simulations for different necking models and coefficients for the monodisperse case.

5.1.1.2. NRMSE Values. NRMSE values are calculated based on Equation (4.9) for both normalized and bulk scattering matrix elements and the results are presented as bar charts in Figure 5.3. The bar charts illustrate the accumulation of NRMSE values associated with specified normalized or bulk scattering matrix elements for distinct necking model-coefficient pairs. The red horizontal line corresponds to the minimum NRMSE among all the accumulated NRMSE values for different necking models and coefficients.

In Figure 5.3a, NRMSE values associated with all normalized and bulk scattering matrix elements are combined for the analysis of the proper necking model. According to Figure 5.3a, the most accurate necking model among all the alternatives is MCCM with $C_{neck} = 0.8$, and the nearest alternative is LFM with $C_{neck} = 0.4$. The differences between NRMSE values of no neck case and MCCM with small C_{neck} are almost indistinguishable. On the other hand, when LFM is used to represent necking, the distinction between different cases becomes more significant, which is expected since the effect of necking is observed to be greater for LFM as compared to that for MCCM. Moreover, the distinctions between NRMSE values corresponding to different necking models and coefficients are more pronounced for S_{11} as compared to the other scattering matrix elements. Additionally, as can be observed from Figure 5.3a, the same results would be obtained if only S_{11} data were used instead of the overall data. Moreover, the distinctions between different necking models are more noticeable. Although NRMSE values associated with the other scattering matrix elements contribute to the evaluation and identification of the proper necking model, their effects are either cancelled by those of other elements or not sufficient to change the resultant necking model based solely on S_{11} data.

Figure 5.3b shows the NRMSE chart based on the 1^{st} combination of elements including $\langle S_{11}^{au} \rangle$, $\langle S_{12}^{au} \rangle$, and $\widetilde{\langle S_{12} \rangle}$. The analysis based on this combination yields MCCM with $C_{neck} = 0.8$ as the most realistic necking model which is consistent with the result obtained from the overall data. The distinctions between different cases are considerable for the bulk scattering matrix elements, and are slightly more pronounced for this

combination due to the necking specific morphology conciseness of the data. It seems that the combination of $\langle S_{11}^{au} \rangle$ and $\langle S_{12}^{au} \rangle$ yields sufficient information for identification of the proper necking model for the monodisperse case. Whereas, considering just $\langle S_{11}^{au} \rangle$, LFM with $C_{neck} = 0.6$ appears as an alternative to MCCM with $C_{neck} = 0.8$, which is slightly different from that obtained from the overall data. Figure 5.3c displays the NRMSE chart obtained for the 2^{nd} combination. Similar to the 1^{st} combination, it results in MCCM with $C_{neck} = 0.8$ being the most realistic necking model. Although relying on the bulk elements $\langle S_{11}^{au} \rangle$ and $\langle S_{22}^{au} \rangle$ yields identical results of the best necking model and necking coefficient, consideration of NRMSE of $\widetilde{\langle S_{22} \rangle}$ helps identify the distinctions between different necking model-coefficient pairs. On the other hand, conducting the analysis over $\langle S_{11}^{au} \rangle$ only produces a different result.

Figure 5.3d illustrates the errors associated with different necking models based on the 3^{rd} combination. The results are consistent with the other charts as the 3^{rd} is a combination of 1^{st} and 2^{nd} combinations. The distinctions between different necking model-coefficient pairs are greater for bulk scattering matrix elements as compared to the normalized data. However, NRMSE values of normalized scattering matrix elements make the resultant errors corresponding to different necking models distinguishable, which narrows down the proper necking models suggested by this combination.

Considering the consistency in the results and challenges with the required experimental setup, conducting the analysis over the normalized and bulk S_{11} data, or the 1^{st} or 2^{nd} combination, would be more efficient for the monodisperse case.

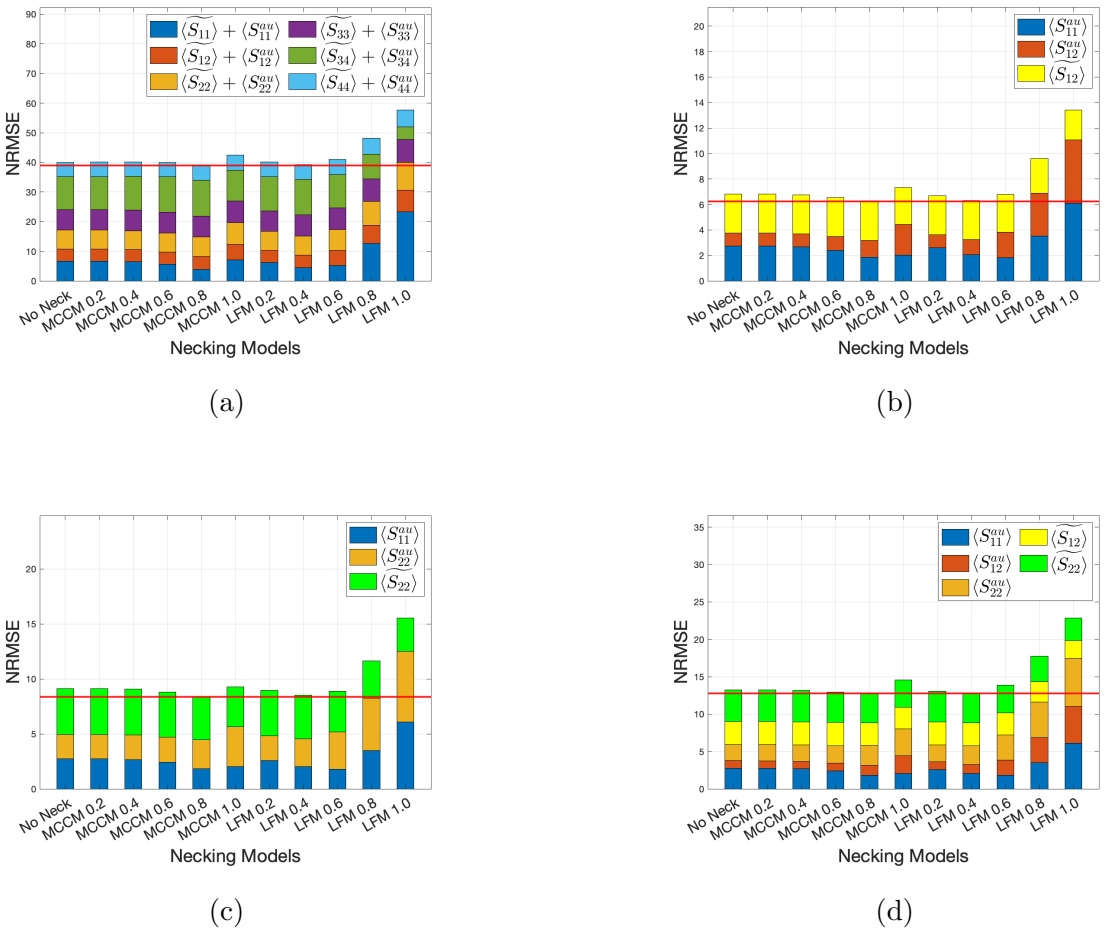

Figure 5.3: Bar charts based on NRMSE values associated with (a) overall normalized and bulk data, (b) 1^{st} suggested combination, (c) 2^{nd} suggested combination, and (d) 3^{rd} suggested combination.

5.1.2. Aggregates Formed by Polydisperse Primary Particles

The results associated with the computed scattering matrix elements for aggregates formed by polydisperse primary particles and evaluation of different necking models based on the predefined error metric, NRMSE, are presented in Sections 5.1.2.1 and 5.1.2.2, respectively.

5.1.2.1. Computed Scattering Matrix Elements. The normalized and bulk scattering matrix element plots for the polydisperse cases are provided in Figure 5.4 and Figure 5.5, respectively. Note that the error bars in the measurement data indicate the standard deviation in the light scattering measurements conducted in a small time interval for each scattering angle. On the other hand, the error bars in the simulation results show the 95% confidence interval deviation in the mean value of the corresponding scattering matrix element. The mean value is derived from the integration of the resultant scattering matrix elements for 10 distinct aggregate representations for each d_{ve}. Considering the fairly small sample size, $N_{frac} = 10$, the student's t-distribution is used to achieve improved statistics for the results of the polydisperse case.

Similar to the monodisperse case, the effect of necking is relatively larger on the normalized scattering matrix elements for LFM than for MCCM as observed in Figure 5.4. The relative effect of necking implemented via MCCM is reduced as compared to the monodisperse case due to the smaller change in the aggregate volume attributed to the definition of MCCM.

The effects of necking on the normalized scattering matrix elements observed in Figure 5.4 are similar to those observed in monodisperse cases. The only difference is observed in the $\widetilde{\langle S_{34} \rangle}$ profile for necking implemented via MCCM; the trend change observed with implementation of necking for the monodisperse cases does not appear for the polydisperse cases. There is a monotonically decreasing trend in the peak value of $\widetilde{\langle S_{34} \rangle}$ for MCCM with increasing C_{neck}. This might be attributed to the structural alteration of the necks represented via MCCM for the polydisperse case, which prevents the space between adjacent primary particles to be completely filled even for the full-neck case possibly leading to changes in the resultant multiple scattering effects. Besides, the deviations associated with different normalized scattering matrix elements are insignificant except for those of $\widetilde{\langle S_{34} \rangle}$, which might be attributed to the sensitivity of S_{34} to polydispersity and the magnitude of S_{34} being too small.

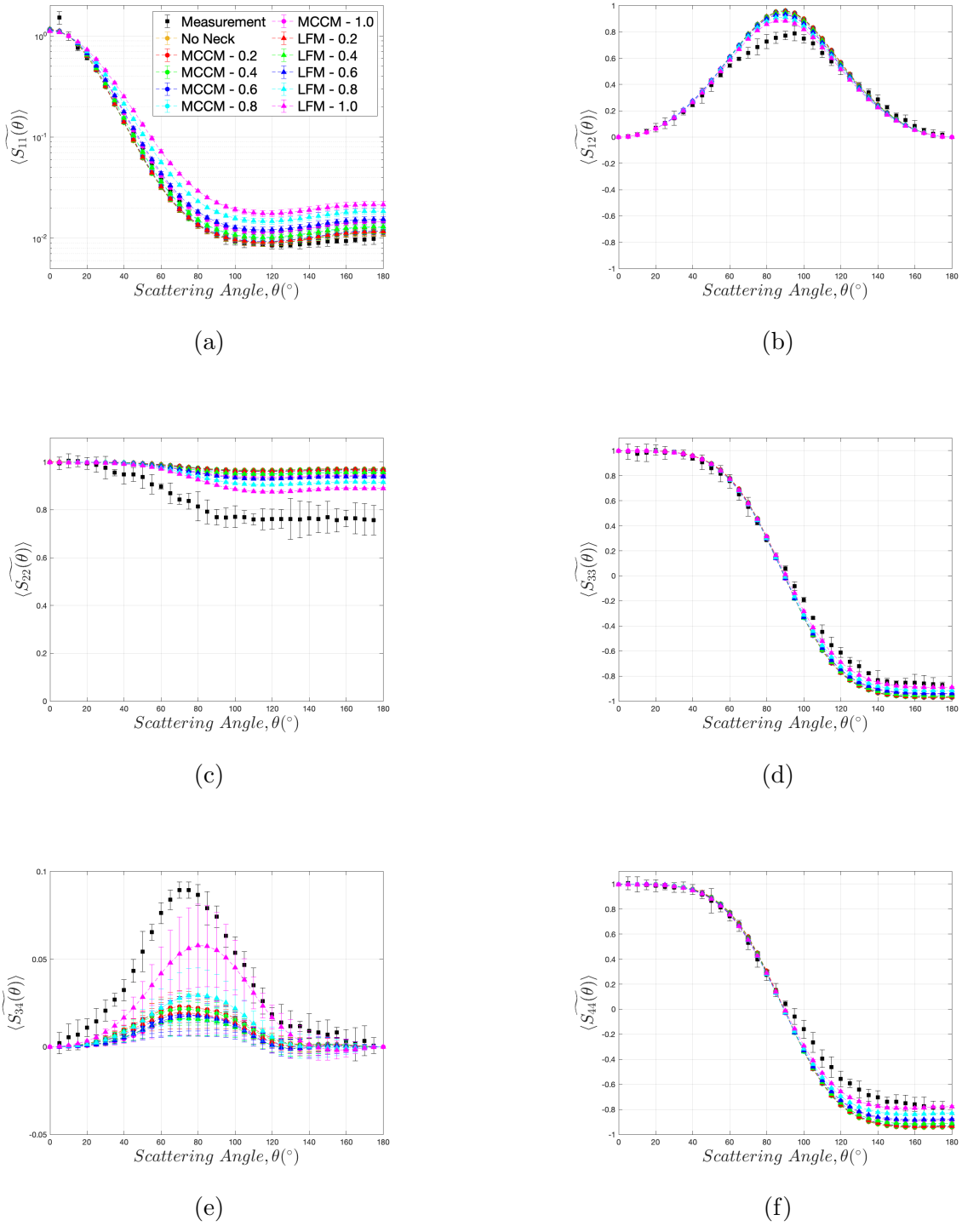

Figure 5.4: Normalized bulk scattering matrix elements obtained from measurement data provided in [26], and DDSCAT simulations for different necking models and coefficients for the polydisperse case.

The effect of necking in Figure 5.5 is observed to be similar to that for the monodisperse case except for the trends in $\langle S_{34}^{au} \rangle$. The change in the trend in $\langle S_{34}^{au} \rangle$ profile due to implementing necking for increasing necking coefficients is annihilated for MCCM, similar to the $\widetilde{\langle S_{34} \rangle}$ plot (Fig 5.4).

The effects of different necking models at different levels on both the normalized and bulk scattering matrix elements seem to be similar to those observed for the monodisperse cases. Although more realistic aggregate representations are generated by considering polydisperse primary particle size distribution, implementing necking to the aggregate representations could not fully recover the deviations in the overall scattering matrix elements for both the normalized and bulk measurement data as can be seen from Figures 5.4 and 5.5. However, there is an improvement in estimating the experimental results with implementation of necking, which might be utilized in identifying the proper necking model for the aggregates of interest. Quantitative analyses are required to determine the most realistic necking model(s).

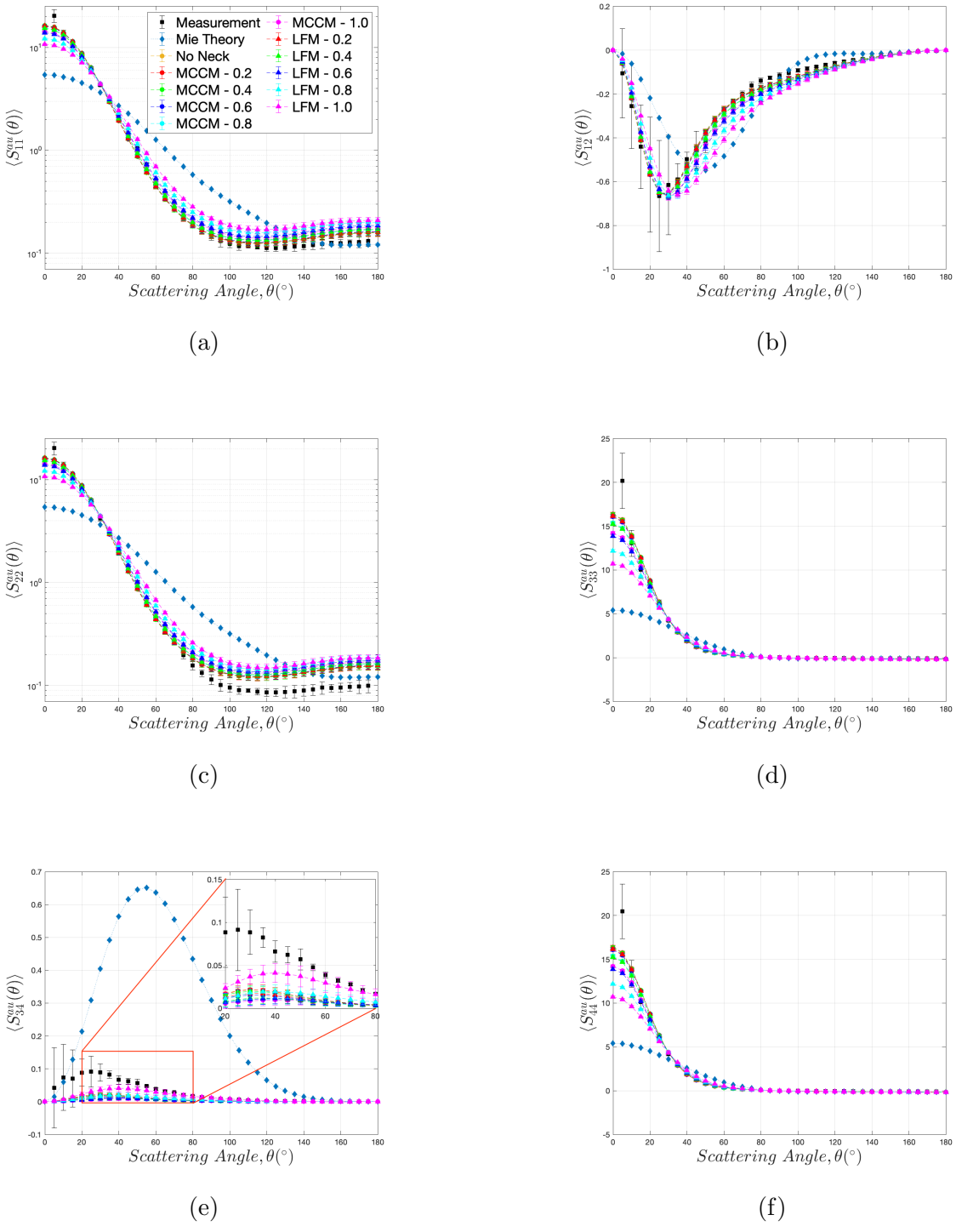

(a) (b)

(c) (d)

(e) (f)

Figure 5.5: Bulk scattering matrix elements obtained from measurement data provided in [26], and DDSCAT simulations for different necking models and coefficients for the polydisperse case.

5.1.2.2. NRMSE Values. NRMSE values for the polydisperse cases are calculated over the mean value of different normalized or bulk scattering matrix elements, $\overline{S_{ij,km}}$, which are obtained by integrating the scattering matrix elements for 10 distinct polydisperse aggregate representations for each d_{ve} sample point and are provided in Figure 5.6.

As can be seen in Figure 5.6a, utilizing overall normalized and bulk data for the polydisperse case yields multiple necking models that resemble the measurement data better than the other alternatives. These are the no neck case, MCCM with $C_{neck} = 0.2$, MCCM with $C_{neck} = 0.4$, MCCM with $C_{neck} = 0.6$, and LFM with $C_{neck} = 0.2$. Apparently, no-necking or smaller necking coefficients are suggested for the polydisperse case when the quantitative analyses are based on the overall normalized and bulk data. This is associated with the change in the aggregate size/volume due to introducing polydispersity to the aggregate representations. In addition, calculating the NRMSE values over the mean values, $\overline{S_{ij,km}}$, might reduce the distinctions between different necking models, and result in multiple alternatives for representing necking accordingly. Nevertheless, the suggested necking models are not too different from those of the monodisperse case since the relative effect of necking is more pronounced than that of polydispersity for this study. The greatest contribution to the distinctions between different necking models is associated with the accumulation of normalized and bulk S_{11}^{au} data. The NRMSE values of normalized and bulk S_{12}^{au} and S_{22}^{au} for different necking models are almost indistinguishable, but they increase the distinctions between alternative models when accumulated with NRMSE of normalized and bulk S_{11}^{au}. The remaining pairs of normalized and bulk elements do not provide significant information in addition to that obtained from the combination of S_{11}^{au}, S_{12}^{au}, and S_{22}^{au} data.

Quantitative analyses based on the suggested error combinations yield similar results to those obtained from the overall normalized and bulk data. Similarly, there are multiple necking models with similar NRMSE values that perform better as compared to the alternatives. The suggested necking models based on the combined errors are the no neck case, MCCM with $C_{neck} = 0.2$, MCCM with $C_{neck} = 0.4$, MCCM with $C_{neck} = 0.6$, and LFM with $C_{neck} = 0.2$. The main contributors of the distinctions between different necking models are the bulk elements.

Table 5.1: Proposed necking models based on various evaluation metrics.

Evaluation Metric	Monodisperse Case	Polydisperse Case
$\widetilde{\langle S_{11} \rangle}$ and $\langle S_{11}^{au} \rangle$	MCCM($C_{neck} = 0.8$)	MCCM($C_{neck} = 0.6, 0.8$) LFM($C_{neck} = 0.2$)
1^{st} Combination	MCCM($C_{neck} = 0.8$) LFM($C_{neck} = 0.4$)	MCCM($C_{neck} = 0.2, 0.4, 0.6$) No Neck, LFM($C_{neck} = 0.2$)
2^{nd} Combination	MCCM($C_{neck} = 0.8$) LFM($C_{neck} = 0.4$)	MCCM($C_{neck} = 0.2, 0.4, 0.6$) No Neck, LFM($C_{neck} = 0.2$)
3^{rd} Combination	MCCM($C_{neck} = 0.8$) LFM($C_{neck} = 0.4$)	MCCM($C_{neck} = 0.2, 0.4, 0.6$) No Neck, LFM($C_{neck} = 0.2$)
Overall Scattering Matrix Elements	MCCM($C_{neck} = 0.8$) LFM($C_{neck} = 0.4$)	MCCM($C_{neck} = 0.2, 0.4, 0.6$) No Neck, LFM($C_{neck} = 0.2$)

Proposed necking models based on different evaluation metrics are summarized in Table 5.1. For the polydisperse case, MCCM with small C_{neck} yields smaller NRMSE values for normalized and bulk scattering matrix elements. Moreover, the structural alteration resulted from the definition of MCCM for the polydisperse case does not change the trend with necking in scattering matrix elements significantly. Therefore, MCCM stands as an alternative for LFM to represent necking in polydisperse aggregates, which is easier to implement. Besides, dipole generation via MCCM takes approximately 657 seconds on average in a 16-core 2.40 GHz processor, which is nearly 28 times faster than that for LFM. Furthermore, considering that the overall normalized and bulk data

might contain redundant morphological information regarding necking, the consistency of the results corresponding to the suggested error combinations, and the challenges with measuring the overall scattering matrix elements experimentally, conducting the analysis of the proper necking model based on the 1^{st} or 2^{nd} combination might be more efficient.

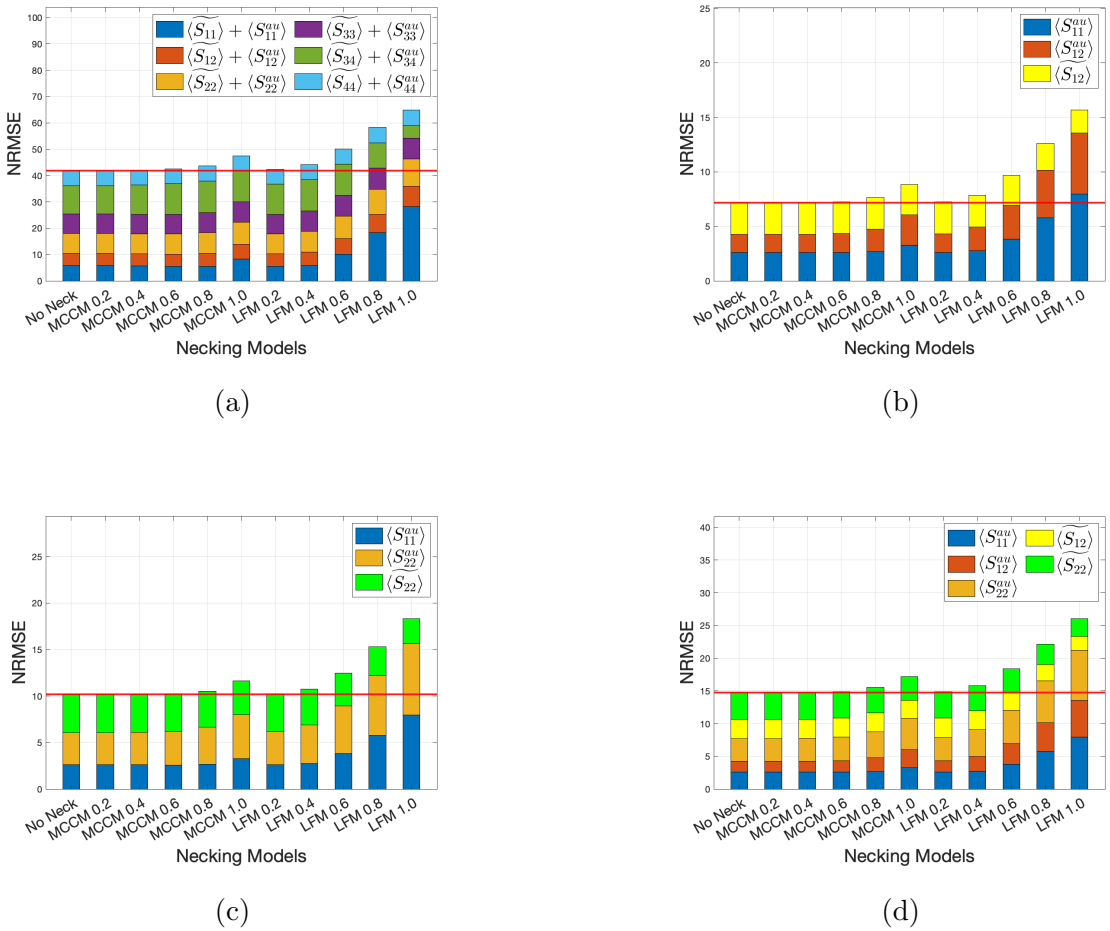

Figure 5.6: Bar charts based on NRMSE values associated with (a) overall normalized and bulk data, (b) 1^{st} suggested combination, (c) 2^{nd} suggested combination, and (d) 3^{rd} suggested combination for the polydisperse case.

5.2. Effects of Necking and Polydispersity in Aggregate and Primary Particle Size on the Scattering Matrix

Effects of necking and polydispersity in aggregate and primary partice size on the scattering matrix are discussed over the resultant scattering matrix element profiles, which are provided in Section 5.2.1. Additionally, the aggregate volume based approach proposed for representing the impact of minor structures on the optical properties of soot aggregates is evaluated based on the scattering matrix elements. Corresponding results and discussions are given in Section 5.2.2.

5.2.1. Computed Scattering Matrix Elements

Computed elements of the scattering matrix elements, S and S^{au}, are provided in Figures 5.7 and 5.8, respectively. The effects of necking and polydispersity in aggregate and primary particle size on the scattering matrix elements are clearly observed in Figure 5.7, where the effect of aggregate volume variation as well as other structural changes are also observed. The error bars in the scattering matrix element plots indicate the 95% confidence interval for the mean value of the corresponding element calculated over a number of aggregate representations based on the student's t-distribution. Overall, the variances in the mean values of the scattering matrix elements are fairly small, except for $\langle S_{34} \rangle$, for which the magnitudes of the mean values are so small that the variances become relatively significant. This might be attributed to the sensitivity of $\langle S_{34} \rangle$ to many other morphological properties such as the granularity of the aggregate [46] that are not tuned during the aggregate generation. Therefore, it is challenging to derive information specific to the influence of the implemented structures based on $\langle S_{34} \rangle$ only. On the other hand, the overall scattering matrix provides a comprehensive information on the impact of necking and polydispersity in aggregate and monomer size on the scattering properties of the aggregates.

The impacts of the considered structures on the scattering matrix are significant as can be seen from Figure 5.7. In general, implementing necking and primary particle polydispersity have similar effects as observed from the trends in Figure 5.7. Furthermore, it seems that the corresponding impacts might be represented by introducing a scaling factor to *Case 1*. The effects of necking and primary particle polydispersity on the scattering matrix are almost identical when necking is implemented via MCCM with $C_{neck} = 0.8$, which might be attributed to their volumes being similar. For larger C_{neck}, the effect of necking dominates that of aggregate and primary particle size polydispersity. On the other hand, introducing aggregate size polydispersity yields a trend change in the resultant scattering profiles. The effects of aggregate size polydispersity on $\langle S_{11} \rangle$, $\langle S_{22} \rangle$, $\langle S_{33} \rangle$, and $\langle S_{44} \rangle$ indicate that asymmetry in the scattering profiles are increased. Implementing polydispersity in aggregate size results in a shift in the location of extremum towards the forward scattering angles for S_{12}. Similarly, aggregate size polydispersity changes the trend of $\langle S_{34} \rangle$ profile by increasing the number of extrema. Therefore, the impact of aggregate size polydispersity on the scattering matrix, S, is more complex than that of necking and primary particle polydispersity, and accounting for its impact might not be straightforward.

In Figure 5.8, the effects of implementing necking and primary particle polydispersity on the elements of S^{au} are fairly small, except for $\langle S^{au}_{34} \rangle$. Observations on $\langle S^{au}_{11} \rangle$, $\langle S^{au}_{22} \rangle$, $\langle S^{au}_{33} \rangle$, and $\langle S^{au}_{44} \rangle$ indicate that relying on the monodisperse primary particle size assumption results in an overestimation at forward scattering angles that can be observed for Case 7 and Case 8. These trends occur due to the structural impacts of polydispersity in primary particle size, which are in agreement with the results presented in Section 5.1. Similar to the effect of primary particle polydispersity, implementing necking results in a decrease in $\langle S^{au}_{11} \rangle$, $\langle S^{au}_{22} \rangle$, $\langle S^{au}_{33} \rangle$, and $\langle S^{au}_{44} \rangle$ at forward scattering angles. The fairly small impacts of necking and primary particle polydispersity might be attributed to the definition of S^{au}, which is S normalized by $C_{sca}k^2/4\pi$. Accordingly, the impact of necking and primary particle polydispersity related to the resultant variation in C_{sca} is obscured due to this normalization. Considering that C_{sca} is highly dependent on the aggregate volume, S^{au} presents the impacts partially isolated from the

resultant volume variation, which can be referred as the *structural impacts*. Thereby, the structural impacts of necking and primary particle polydispersity are similar but minor based on the observations on Figure 5.8. However, the structural impact of aggregate size polydispersity is observed to be significant, which implies that the impact of polydispersity in aggregate size is not dominated by the resultant aggregate volume variation. This is in contrast to impact of necking and primary particle polydispersity. Observations on $\langle S_{11}^{au} \rangle$, $\langle S_{22}^{au} \rangle$, $\langle S_{33}^{au} \rangle$, and $\langle S_{44}^{au} \rangle$ demonstrate that the asymmetry in the scattering profiles increases with implementation of polydispersity in aggregate size. These trends are opposite to those of implementing necking and primary particle polydispersity. Furthermore, the extremum of $\langle S_{12}^{au} \rangle$ shifts towards smaller scattering angles with the implementation of aggregate size polydispersity, which yields a disrupted symmetry of the scattering profile.

The trends observed in $\langle S_{34} \rangle$ and $\langle S_{34}^{au} \rangle$ differentiate from those of other elements. Implementing necking with larger C_{neck} results in a decrease in the peak $\langle S_{34} \rangle$ and $\langle S_{34}^{au} \rangle$ value, whereas implementing polydispersity in primary particle size yields the opposite trend. However, the variances in $\langle S_{34} \rangle$ and $\langle S_{34}^{au} \rangle$ are too large such that it is difficult to distinguish the individual impacts of necking and primary particle polydispersity.

Comparison of the effects of polydispersity in aggregate size and primary particle size indicates that the overall impacts are comparable, whereas the structural impact of aggregate size polydispersity is much more pronounced than that of primary particle polydispersity. These results are in agreement with the study of Farias et al. [19] demonstrating that the effect of aggregate size polydispersity on the optical properties is more enhanced than that of primary particle polydispersity. However, in the studies by Charalampopoulos and Shu [20] and F. Liu et al. [21], the impact of aggregate size polydispersity on the optical properties was observed to be less significant as compared to that of primary particle polydispersity. This might be attributed to the differences in morphology of the considered structures, and the optical quantities of interest. Charalampopoulos and Shu [20] considered chain-like aggregates with relatively small number of primary particles, which might reduce the impact of aggregate

size polydispersity considering the asymmetric structure of these aggregates. F. Liu et al. [21] used LII method to investigate the impact of polydispersity in aggregate and primary particle size based on the observations of the resultant temperature profile. Although the change in the temperature profile provide information on the size/volume effects, it might not provide comprehensive information on the structural impacts. Accordingly, LII might underestimate the potential impact of aggregate size polydispersity on the optical properties as the structural impact of aggregate size polydispersity is found to be significant.

Observations on the scattering matrix elements provided in Figures 5.7 and 5.8 demonstrate that the overall impacts of necking and polydispersity in aggregate and primary particle size are significant. Therefore, these structures should be considered in the aggregate models to improve the accuracy of in-situ optical diagnostic methods. Moreover, the impacts associated with implementing necking and primary particle polydispersity are mainly due to the resultant variation in the scattering cross-section, which is governed by the aggregate volume variation. Accordingly, the aggregate volume based approach seems a reasonable method to account for the effect of necking and primary particle polydispersity on scattering matrix elements. On the other hand, the influence of aggregate size polydispersity is observed to be more complicated than the other structures.

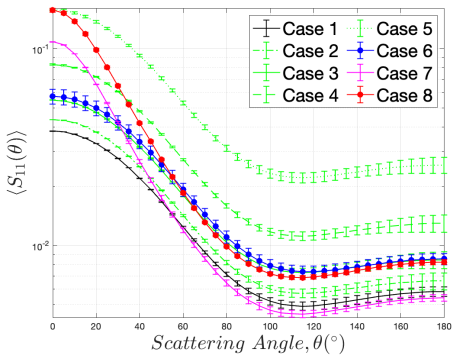

(a)

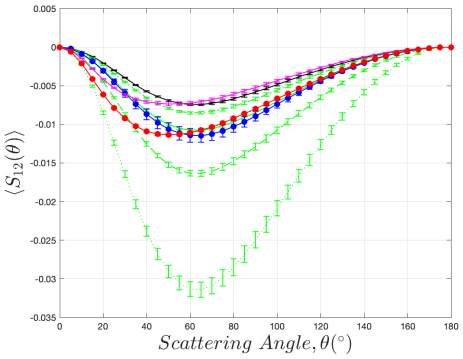

(b)

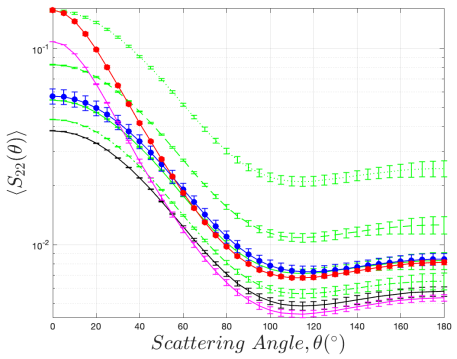

(c)

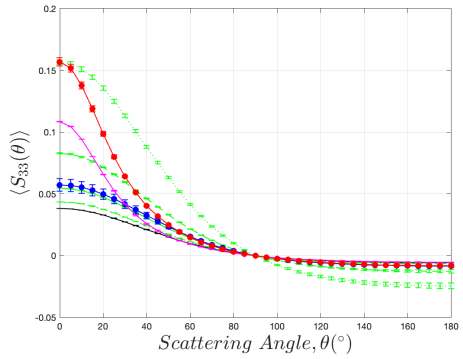

(d)

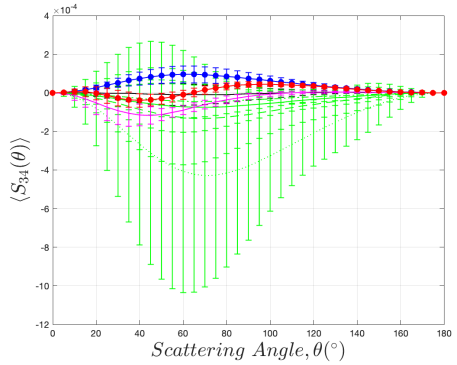

(e)

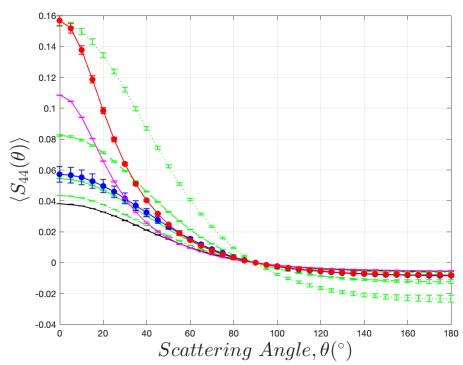

(f)

Figure 5.7: Elements of the scattering matrix S for the specified cases.

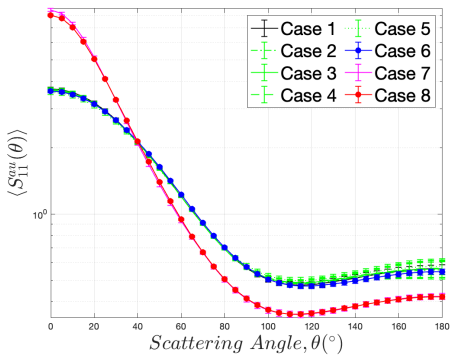

(a)

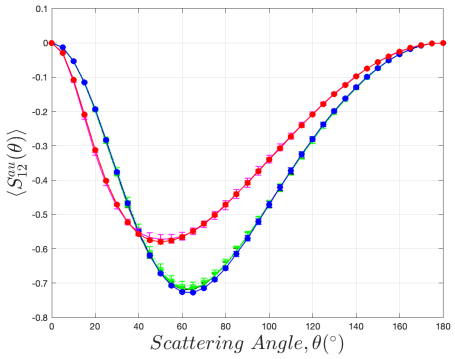

(b)

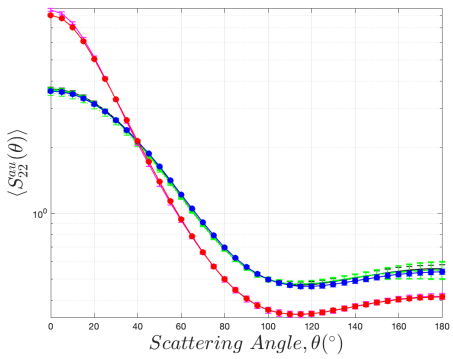

(c)

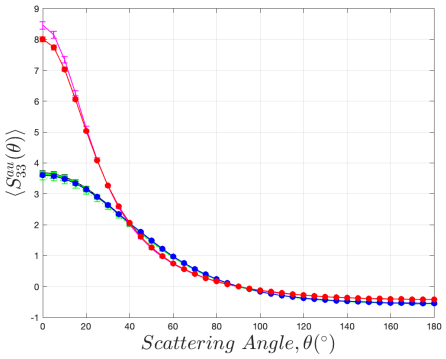

(d)

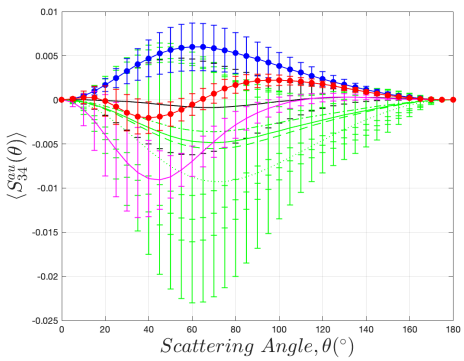

(e)

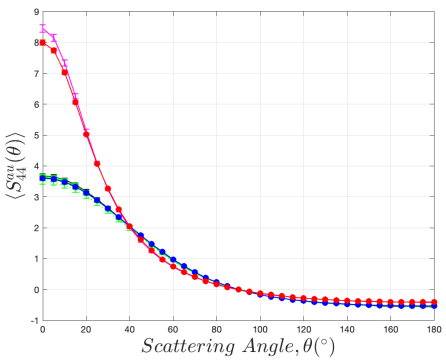

(f)

Figure 5.8: Elements of the scattering matrix S^{au} for the specified cases.

5.2.2. Evaluation of Aggregate Volume Based Approach

The aggregate volume based approach for representing the impact of necking on the resultant scattering properties is evaluated through a comparison of the elements of the scattering matrix, S. Necking is implemented based on the constant monomer radius approach (CMRA) and the constant aggregate volume approach (CAVA), which were explained earlier in Section 4.2.2. The effect of aggregate volume variation due to implementation of necking is eliminated with CAVA and the resultant scattering matrix element profiles are compared with those of Case 1. Accordingly, the impact of necking on the scattering matrix isolated from the resultant change in the aggregate volume is observed and the accuracy of the aggregate volume based approach is evaluated. Cases 2, 3, and 4 are considered to evaluate the aggregate volume based approach in estimating the impact of necking. However, only the results of Case 4, where necking is implemented via MCCM with $C_{neck} = 1.0$, are presented, since similar behaviors are observed for the other cases. The resultant scattering matrix elements are shown in Figure 5.9. The scattering matrix elements of Case 1 and Case 4 based on CAVA yield very similar results, except for $\langle S_{34} \rangle$ as can be seen in Figure 5.9. Although the $\langle S_{34} \rangle$ profile associated with Case 4 approximates that of Case 1 when CAVA is introduced, there are still observable deviations. However, the variances in the mean values of $\langle S_{34} \rangle$ are larger than these deviations, which makes it difficult to distinguish the profiles for different cases. Altogether, the effect of necking on the scattering matrix elements seems to be governed by the resultant aggregate volume variation. However, there are slight differences between the profiles for Case 1 and Case 4 based on CAVA, which are attributed to the structural impacts of implementing necking to the aggregate representations. This observation is consistent with the scattering matrix element profiles shown in Figure 5.8, where the impacts partially isolated from the resultant volume variation are observed. Therefore, the aggregate volume based approach fails to account for the structural impacts of necking on the scattering matrix element profiles.

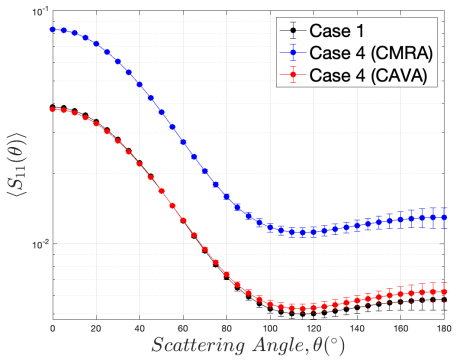

(a)

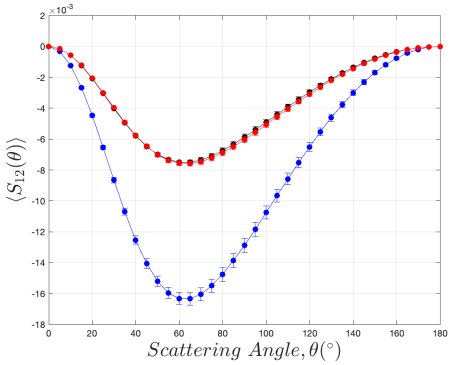

(b)

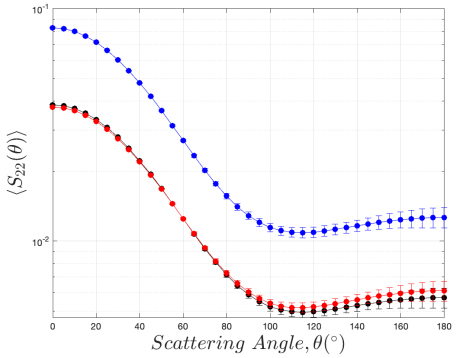

(c)

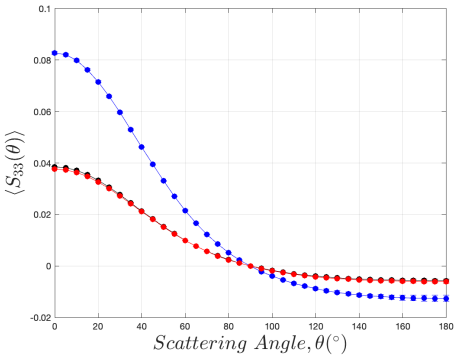

(d)

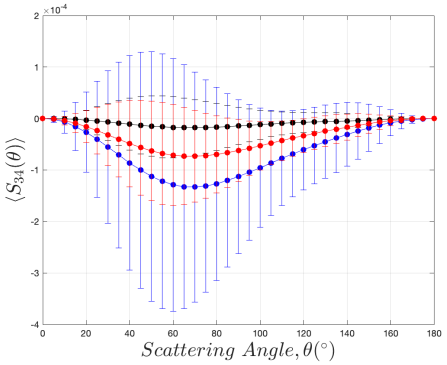

(e)

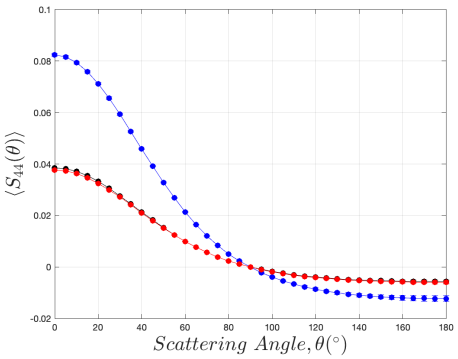

(f)

Figure 5.9: Elements of the scattering matrix S for Case 1 and Case 4 based on constant monomer radius approach (CMRA) and constant aggregate volume approach (CAVA).

Overall, the aggregate volume based approach yields sufficiently accurate approximations of the effect of necking on the scattering matrix elements for the cases investigated in this study. However, the accuracy of approximations might be reduced for aggregates with different morphological properties for which the structural impacts of necking on the scattering matrix elements are significant, as in Section 5.1. Accordingly, relying on the aggregate volume based approach to account for the impact of necking and primary particle polydispersity would be misleading for such cases. Therefore, an improved model representing the structural impacts of these structures as well as the impacts originated from the resultant volume variation might be required.

The structural impacts of necking and primary particle polydispersity might be investigated over the resultant S^{au} profiles, which can be characterized based on the asymmetry factor, g. Observation of the $\langle S_{11}^{au} \rangle$ profiles in Figure 5.8 indicates that the symmetry in the scattering profile is generally improved when necking or primary particle polydispersity is introduced. This observation is in agreement with the results presented by Yon et al. [24] and observations provided in Section 5.1. Based on the observations of Figure 5.8, the impact of necking and primary particle polydispersity on $\langle S^{au} \rangle$ profiles might be related to the compactness of the aggregates. The radius of gyration of the aggregate, R_g, might be used as a characteristic parameter identifying the aggregate compactness. Accordingly, the resultant variation in R_g might be utilized in approximating the impact of necking and primary particle polydispersity on $\langle S^{au} \rangle$, as proposed in Section 5.1.1.1. The comparison of the resultant R_g and g associated with different cases provide a quantitative analysis of the relation between the radius of gyration and the structural impacts of necking and primary particle polydispersity.

The radii of gyration and the asymmetry factors for Cases 1-8 are calculated based on Equation (4.11) and Equation (4.10), respectively. The mean values of the radii of gyration and the asymmetry factors at 95% confidence intervals for the considered cases are provided in Table 5.2. Note that the statistics are calculated over 10 or 30 aggregate representations generated based on the same set of morphological parameters for the cases of monodisperse and polydisperse monomer size distribution, respectively.

As can be seen from Table 5.2, implementing necking and polydispersity in primary particle size decreases the radius of gyration and the asymmetry factor in general. This indicates that the radius of gyration of the aggregates and the symmetry of the resultant scattering profiles seem to be related, which is in agreement with Yon et al. [24]. While there exists an exception for Case 6, where the mean value of g is slightly increased as compared to Case 1, the asymmetry factors are almost indistinguishable considering the corresponding confidence intervals. Moreover, g cannot completely characterize the individual impacts of necking and primary particle polydispersity on the resultant scattering profile. For example, $\langle S_{11}^{au} \rangle$ values at small scattering angles ($\theta < 30^{\circ}$) are commonly decreased when necking or primary particle polydispersity is introduced. Therefore, there is a similarity between the impacts of necking and primary particle polydispersity on the resultant scattering profile.

Table 5.2: Radii of gyration and asymmetry factors for the considered cases.

Cases	Radius of Gyration, R_g (nm)	Asymmetry Factor, g
1	123.2 ± 0.0	0.3629 ± 0.0111
2	123.0 ± 0.0	0.3610 ± 0.0115
3	122.5 ± 0.0	0.3576 ± 0.0116
4	122.1 ± 0.2	0.3555 ± 0.0119
5	120.3 ± 0.5	0.3477 ± 0.0118
6	117.4 ± 1.6	0.3655 ± 0.0085
7	228.1 ± 0.9	0.5022 ± 0.0079
8	216.5 ± 1.5	0.4996 ± 0.0042

Altogether, the data on Table 5.2 imply that the resultant changes in the trends of the scattering profiles are correlated with those of the radius of gyration. Therefore, establishing the relation between R_g and $\langle S^{au} \rangle$ for necking and primary particle polydispersity might be utilized in representing the corresponding structural impacts. Accordingly, the scattering properties of the aggregates can be approximated more accurately without conducting scattering simulations over complex aggregate structures

including necking and primary particle polydispersity. Moreover, the structural impact of aggregate size polydispersity might be approximated based on the resultant change in R_g as well. Further studies on the relation between the impacts of these structural effects and the resultant variations in the radius of gyration and the aggregate volume are required to develop accurate models to account for the corresponding influences on the scattering properties.

6. CONCLUSION

In this study, a comprehensive analysis of the effects of necking and polydispersity in aggregate and primary particle size in flame-soot aggregates is conducted to investigate their influences on scattering matrix elements. Additionally, a methodology is developed to analyze the accuracy of different necking models based on measured scattering matrix elements quantitatively, and enable more accurate estimations of their impact on the optical properties accordingly. Aggregate representations are generated via tunable fractal generation algorithms utilizing particle-cluster and cluster-cluster aggregation based on typical morphological parameters associated with soot aggregates derived from the literature. Necking is implemented via a modified cylindrical connector model (MCCM) and the 3D level-set function model (LFM) with different coefficients, C_{neck}. Aggregate and primary particle polydispersity are implemented based on log-normal distribution. The individual impacts of these structures are investigated based on the resultant profiles of the elements of S and S^{au}. Furthermore, the aggregate volume based approach is evaluated for representing the impact of necking on the scattering matrix elements. Additionally, the relation between the radius of gyration and the trends of S^{au} characterized by the asymmetry factor is presented for the specified cases.

The following conclusions are drawn from the analysis of different necking models in predicting measured scattering matrix elements of soot aggregates:

- MCCM with $C_{neck} = 0.8$ exhibited the best performance in approximating the experimental data with the nearest alternative of LFM with $C_{neck} = 0.4$ for the monodisperse case. Implementing polydispersity to primary particles of the aggregates results in small changes in the necking coefficients associated with the proposed necking models. Therefore, relying merely on the assumption of monodisperse primary particles for the analysis of different necking models would be misleading.

- The structural effects of implementing necking via LFM and MCCM on the scattering matrix elements are found to be similar for aggregates formed by both monodisperse and polydisperse primary particles. Considering its simplicity and computational efficiency, modeling necking in soot aggregates via MCCM seems to be a more feasible approach if the amount of necking is not excessive.
- Although S_{34} is very sensitive to implementation of necking, deriving information specific to necking might be challenging since it is also sensitive to many other morphological parameters. Besides, the precision in the measurement data should be high as the magnitudes of S_{34} are too small.
- The combinations $\left(\langle S_{11}^{au}\rangle, \langle S_{12}^{au}\rangle, \widetilde{\langle S_{12}\rangle}\right)$ and $\left(\langle S_{11}^{au}\rangle, \langle S_{22}^{au}\rangle, \widetilde{\langle S_{22}\rangle}\right)$ stand out as adoptable metrics for necking characterization utilizing different polarization states of the incident light.
- For the monodisperse case, analysis based on S_{11} that can be obtained from measurements of unpolarized light yields the same result produced by the analyses based on the suggested metrics. For the polydisperse cases, analysis based on S_{11} could not provide sufficient morphological information such that the distinctions between different necking models are diminished as compared to the analyses based on the suggested metrics. Accordingly, the proposed necking models appeared to be slightly different from those obtained from the suggested evaluation metrics. Although measurements for unpolarized light supply significant information on the level of necking in the aggregate, measurements for different polarization states are required to increase the fidelity of characterization of necking.
- The overall impacts of necking and polydispersity in aggregate and primary particle size on the scattering matrix elements are significant. Therefore, these structures need to be considered to achieve more accurate morphological diagnosis and high fidelity optical characterization methods for soot aggregates accordingly.

- Although there are improvements in predicting the experimental data with implementation of necking, the deviations from the measurement data could not be completely annihilated. This might be associated with the alterations in the morphology of the aggregates through the treatments of sampling, which possibly result in modification of certain morphological parameters.

According to the investigation of the effect of necking and polydispersity in aggregate and primary particle size on the scattering matrix elements:

- The impacts of necking and primary particle polydispersity on the scattering matrix elements are mainly due to the resultant aggregate volume variation.
- The effect of aggregate polydispersity on the scattering matrix elements is more complicated than that of necking and primary particle polydispersity.
- The aggregate volume based approach shows adequate performance in accounting for the impact of necking on the scattering matrix elements for the specified cases. However, it cannot represent the structural impacts of these structures. Accordingly, the accuracy of scattering properties estimated based on this approach might be significantly reduced for the cases where the structural impacts become important.
- The radius of gyration seems to be correlated with the trends of S^{au} profiles characterized by the asymmetry factor. Therefore, the structural impacts of necking and polydispersity in aggregate and primary particle size might be represented based on the resultant variation in the radius of gyration.

Overall, relation between morphology and scattering properties of soot aggregates is outlined as identifying this relation is crucial to determine the key parameters that define the aggregate morphology and provide comprehensive information on the optical properties. Accordingly, more accurate and efficient methods for optical characterization of soot aggregates can be developed.

Resultant variations in the volume and radius of gyration of the aggregates stand out as promising metrics for representing the impacts of necking and polydispersity in aggregate and primary particle size on the scattering matrix. Future studies might focus on establishing the relation between the radius of gyration and the scattering matrix, S^{au}, for aggregates with different morphological parameters. Accordingly, the improvement introduced to the volume based approach by considering the resultant variation in the radius of gyration can be evaluated. Based on these studies, the impact of necking and polydispersity in aggregate and primary particle size on the scattering matrix might be accurately represented.

REFERENCES

1. Kennedy, I. M., "The Health Effects of Combustion-Generated Aerosols", *Proceedings of the Combustion Institute*, Vol. 31, No. 2, pp. 2757–2770, 2007.

2. Perera, F., A. Ashrafi, P. Kinney and D. Mills, "Towards a Fuller Assessment of Benefits to Children's Health of Reducing Air Pollution and Mitigating Climate Change due to Fossil Fuel Combustion", *Environmental Research*, Vol. 172, pp. 55–72, 2019.

3. Ramanathan, V. and G. Carmichael, "Global and Regional Climate Changes due to Black Carbon", *Nature Geoscience*, Vol. 1, No. 4, pp. 221–227, 2008.

4. Bond, T. C., S. J. Doherty, D. W. Fahey, P. M. Forster, T. Berntsen, B. J. DeAngelo, M. G. Flanner, S. Ghan, B. Kärcher, D. Koch *et al.*, "Bounding the Role of Black Carbon in the Climate System: A Scientific Assessment", *Journal of Geophysical Research: Atmospheres*, Vol. 118, No. 11, pp. 5380–5552, 2013.

5. Daun, K. J., B. J. Stagg, F. Liu, G. J. Smallwood and D. R. Snelling, "Determining Aerosol Particle Size Distributions Using Time-Resolved Laser-Induced Incandescence", *Applied Physics B*, Vol. 87, No. 2, pp. 363–372, 2007.

6. Talebi-Moghaddam, S., F. J. Bauer, F. J. T. Huber, S. Will and K. J. Daun, "Inferring Soot Morphology Through Multi-Angle Light Scattering Using an Artificial Neural Network", *Journal of Quantitative Spectroscopy and Radiative Transfer*, Vol. 251, Article 106957, 2020.

7. Eriçok, O. B. and H. Ertürk, "Inverse Characterization of Nanoparticle Clusters Using Unpolarized Optical Scattering Without Ex-Situ Measurements", *Journal of Quantitative Spectroscopy and Radiative Transfer*, Vol. 198, pp. 117–129, 2017.

8. Tian, K., F. Liu, K. A. Thomson, D. R. Snelling, G. J. Smallwood and D. Wang,

"Distribution of the Number of Primary Particles of Soot Aggregates in a Non-premixed Laminar Flame", *Combustion and Flame*, Vol. 138, No. 1, pp. 195–198, 2004.

9. Burr, D. W., K. J. Daun, O. Link, K. A. Thomson and G. J. Smallwood, "Determination of the Soot Aggregate Size Distribution From Elastic Light Scattering Through Bayesian Inference", *Journal of Quantitative Spectroscopy and Radiative Transfer*, Vol. 112, No. 6, pp. 1099–1107, 2011.

10. Gwaze, P., O. Schmida, H. J. Annegarnb, M. O. Andreaea, J. Huthc and G. Helas, "Comparison of Three Methods of Fractal Analysis Applied to Soot Aggregates From Wood Combustion", *Journal of Aerosol Science*, Vol. 37, No. 7, pp. 820–838, 2006.

11. Chakrabarty, R. K., H. Moosmüller, W. P. Arnott, M. A. Garro, G. Tian, J. G. Slowik, E. S. Cross, J.-H. Han, P. Davidovits, T. B. Onasch and D. R. Worsnop, "Low Fractal Dimension Cluster-Dilute Soot Aggregates From a Premixed Flame", *Physical Review Letters*, Vol. 102, Article 235504, 2009.

12. Wang, Y., F. Liu, C. He, L. Bi, T. Cheng, Z. Wang, H. Zhang, X. Zhang, Z. Shi and W. Li, "Fractal Dimensions and Mixing Structures of Soot Particles During Atmospheric Processing", *Environmental Science & Technology Letters*, Vol. 4, No. 11, pp. 487–493, 2017.

13. Pirjola, L., J. V. Niemi, S. Saarikoski, M. Aurela, J. Enroth, S. Carbone, K. Saarnio, H. Kuuluvainen, A. Kousa, T. Rönkkö and R. Hillamo, "Physical and Chemical Characterization of Urban Winter-Time Aerosols by Mobile Measurements in Helsinki, Finland", *Atmospheric Environment*, Vol. 158, pp. 60–75, 2017.

14. Bescond, A., J. Yon, T. Girasole, C. Jouen, C. Roze and A. Coppalle, "Numerical Investigation of the Possibility to Determine the Primary Particle Size of Fractal

Aggregates by Measuring Light Depolarization", *Journal of Quantitative Spectroscopy and Radiative Transfer*, Vol. 126, pp. 130–139, 2013.

15. Sorensen, C. M., "Light Scattering by Fractal Aggregates: A Review", *Aerosol Science and Technology*, Vol. 35, No. 2, pp. 648–687, 2001.

16. Mackowski, D. W. and M. I. Mishchenko, "Calculation of the T Matrix and the Scattering Matrix for Ensembles of Spheres", *Journal of the Optical Society of America A*, Vol. 13, No. 11, pp. 2266–2278, 1996.

17. Draine, B. T. and P. J. Flatau, "Discrete-Dipole Approximation for Scattering Calculations", *Journal of the Optical Society of America A*, Vol. 11, No. 4, pp. 1491–1499, 1994.

18. Yon, J., F. Liu, A. Bescond, C. Caumont-Prim, C. Rozé, F.-X. Ouf and A. Coppalle, "Effects of Multiple Scattering on Radiative Properties of Soot Fractal Aggregates", *Journal of Quantitative Spectroscopy and Radiative Transfer*, Vol. 133, pp. 374–381, 2014.

19. Farias, T. L., Ü. Köylü and M. G. Carvalho, "Effects of Polydispersity of Aggregates and Primary Particles on Radiative Properties of Simulated Soot", *Journal of Quantitative Spectroscopy and Radiative Transfer*, Vol. 55, No. 3, pp. 357–371, 1996.

20. Charalampopoulos, T. T. and G. Shu, "Effects of Polydispersity of Chainlike Aggregates on Light-Scattering Properties and Data Inversion", *Applied Optics*, Vol. 41, No. 4, pp. 723–733, 2002.

21. Liu, F., M. Yang, F. A. Hill, D. R. Snelling and G. J. Smallwood, "Influence of Polydisperse Distributions of Both Primary Particle and Aggregate Size on Soot Temperature in Low-Fluence LII", *Applied Physics B*, Vol. 83, No. 3, pp. 383–395, 2006.

22. Liu, C., Y. Yin, F. Hu, H. Jin and C. M. Sorensen, "The Effects of Monomer Size Distribution on the Radiative Properties of Black Carbon Aggregates", *Aerosol Science and Technology*, Vol. 49, No. 10, pp. 928–940, 2015.

23. Skorupski, K. and J. Mroczka, "Effect of the Necking Phenomenon on the Optical Properties of Soot Particles", *Journal of Quantitative Spectroscopy and Radiative Transfer*, Vol. 141, pp. 40–48, 2014.

24. Yon, J., A. Bescond and F. Liu, "On the Radiative Properties of Soot Aggregates Part 1: Necking and Overlapping", *Journal of Quantitative Spectroscopy and Radiative Transfer*, Vol. 162, pp. 197–206, 2015.

25. Teng, S., C. Liu, M. Schnaiter, R. K. Chakrabarty and F. Liu, "Accounting for the Effects of Nonideal Minor Structures on the Optical Properties of Black Carbon Aerosols", *Atmospheric Chemistry and Physics*, Vol. 19, No. 5, pp. 2917–2931, 2019.

26. Liu, J., Q. Zhang, J. Wang and Y. Zhang, "Light Scattering Matrix for Soot Aerosol: Comparisons Between Experimental Measurements and Numerical Simulations", *Journal of Quantitative Spectroscopy and Radiative Transfer*, Vol. 246, Article 106946, 2020.

27. Bao, Y., Y. Huang and B. He, "Impact of Absorptivity and Wavelength on the Optical Properties of Aggregates With Sintering Necks", *Journal of Quantitative Spectroscopy and Radiative Transfer*, Vol. 209, pp. 103–112, 2018.

28. Bao, Y., Y. Huang, W. Li and K. Zhu, "Comparison of the Scattering Properties Between TiO2 and ITO Clusters Based on the Particle Superposition Model", *Optical Material Express*, Vol. 9, No. 2, pp. 562–575, 2019.

29. Yon, J., F. Liu, J. Morán and A. Fuentes, "Impact of the Primary Particle Polydispersity on the Radiative Properties of Soot Aggregates", *Proceedings of the*

Combustion Institute, Vol. 37, No. 1, pp. 1151–1159, 2019.

30. Manickavasagam, S., M. P. Mengüç, Z. Drozdowicz and C. Ball, "Size, Shape, and Structure Analysis of Fine Particles", *American Ceramic Society Bulletin*, Vol. 82, pp. 29–33, 2002.

31. Aslan, M. M., M. P. Mengüç, S. Manickavasagam and C. Saltiel, "Size and Shape Prediction of Colloidal Metal Oxide MgBaFeO Particles From Light Scattering Measurements", *Journal of Nanoparticle Research*, Vol. 8, No. 6, pp. 981–994, 2006.

32. Mengüç, M. P., "Engineering With and for Light Absorption and Scattering: A Quarter Century of Experimental Research at RTL", *ELS XIII Conference, Atti della Accademia Peloritana dei Pericolanti - Classe di Scienze Fisiche, Matematiche e Naturali*, Vol. 89, Taormina, Italy, 2011.

33. Mengüç, M. P. and S. Manickavasagam, "Non-Intrusive Method and Apparatus for Characterizing Particles Based on Scattering Matrix Elements Measurements Using Elliptically Polarized Radiation", U.S. Patent 2002/0057433 A1, May 12, 2002, https://patents.google.com/patent/US20020057433, Accessed on February 8, 2023.

34. Muñoz, O., F. Moreno, D. Guirado, J. L. Ramos, A. López, F. Girela, J. M. Jerónimo, L. P. Costillo and I. Bustamante, "Experimental Determination of Scattering Matrices of Dust Particles at Visible Wavelengths: The IAA Light Scattering Apparatus", *Journal of Quantitative Spectroscopy and Radiative Transfer*, Vol. 111, No. 1, pp. 187–196, 2010.

35. Eriçok, O. B., H. Ertürk and A. T. Cemgil, "Approximate Bayesian Computation Techniques for Optical Characterization of Nanoparticle Clusters", *Journal of the Optical Society of America A*, Vol. 35, pp. 88–97, 2018.

36. Eriçok, O. B. and H. Ertürk, "Optical Characterization Limits of Nanoparticle Aggregates at Different Wavelengths Using Approximate Bayesian Computation", *Journal of Quantitative Spectroscopy and Radiative Transfer*, Vol. 213, pp. 113–118, 2018.

37. Eriçok, O. B., A. K. Özbek, A. T. Cemgil and H. Ertürk, "Gaussian Process and Design of Experiments for Surrogate Modeling of Optical Properties of Fractal Aggregates", *Journal of Quantitative Spectroscopy and Radiative Transfer*, Vol. 239, Article 106643, 2019.

38. Meakin, P., "A Historical Introduction to Computer Models for Fractal Aggregates", *Journal of Sol-Gel Science and Technology*, Vol. 15, No. 2, pp. 97–117, 1999.

39. Filippov, A. V., M. Zurita and D. E. Rosner, "Fractal-Like Aggregates: Relation Between Morphology and Physical Properties", *Journal of Colloid and Interface Science*, Vol. 229, No. 1, pp. 261–273, 2000.

40. Skorupski, K., J. Mroczka, T. Wriedt and N. Riefler, "A Fast and Accurate Implementation of Tunable Algorithms Used for Generation of Fractal-Like Aggregate Models", *Physica A*, Vol. 404, pp. 106–117, 2014.

41. Moran, J., A. Fuentes, F. Liu and J. Yon, "FracVAL: An Improved Tunable Algorithm of Cluster–Cluster Aggregation for Generation of Fractal Structures Formed by Polydisperse Primary Particles", *Computer Physics Communications*, Vol. 239, pp. 225–237, 2019.

42. Dastanpour, R. and S. N. Rogak, "The Effect of Primary Particle Polydispersity on the Morphology and Mobility Diameter of the Fractal Agglomerates in Different Flow Regimes", *Journal of Aerosol Science*, Vol. 94, pp. 22–32, 2016.

43. Mishchenko, M. I., J. W. Hovenier and L. D. Travis, *Light Scattering by Non-*

spherical Particles: Theory, Measurements, and Applications, Academic Press, San Diego, 2000.

44. Klusek, C., S. Manickavasagam and M. P. Mengüç, "Compendium of Scattering Matrix Element Profiles for Soot Agglomerates", *Journal of Quantitative Spectroscopy and Radiative Transfer*, Vol. 79-80, pp. 839–859, 2003.

45. Bohren, C. F. and D. R. Huffman, *Absorption and Scattering of Light by Small Particles*, John Wiley & Sons, Mörlenbach, 1983.

46. Manickavasagam, S. and P. Mengüç, "Scattering Matrix Elements of Fractal-Like Soot Agglomerates", *Applied Optics*, Vol. 36, No. 6, pp. 1337–1351, 1997.

47. Wu, Y., T. Cheng, X. Gu, L. Zheng, H. Chen and H. Xu, "The Single Scattering Properties of Soot Aggregates With Concentric Core–Shell Spherical Monomers", *Journal of Quantitative Spectroscopy and Radiative Transfer*, Vol. 135, pp. 9–19, 2014.

48. Appel, J., H. Bockhorn and M. Frenklach, "Kinetic Modeling of Soot Formation With Detailed Chemistry and Physics: Laminar Premixed Flames of C2 Hydrocarbons", *Combustion and Flame*, Vol. 121, No. 1, pp. 122–136, 2000.

49. Bescond, A., J. Yon, F. X. Ouf, D. Ferry, D. Delhaye, D. Gaffié, A. Coppalle and C. Rozé, "Automated Determination of Aggregate Primary Particle Size Distribution by TEM Image Analysis: Application to Soot", *Aerosol Science and Technology*, Vol. 48, No. 8, pp. 831–841, 2014.

50. Wei, J., Y. Zeng, M. Pan, Y. Zhuang, L. Qiu, T. Zhou and Y. Liu, "Morphology Analysis of Soot Particles From a Modern Diesel Engine Fueled With Different Types of Oxygenated Fuels", *Fuel*, Vol. 267, Article 117248, 2020.

51. Brasil, A. M., T. L. Farias and M. G. Carvalho, "Evaluation of the Fractal Properties of Cluster-Cluster Aggregates", *Aerosol Science and Technology*, Vol. 33,

No. 5, pp. 440–454, 2000.

52. Chang, H.-C. and T. T. Charalampopoulos, "Determination of the Wavelength Dependence of Refractive Indices of Flame Soot", *Proceedings of the Royal Society A*, Vol. 430, No. 1880, pp. 577–591, 1990.

53. Mätzler, C., "MATLAB Functions for Mie Scattering and Absorption", Research Report No. 2002-08, Institute of Applied Physics, University of Bern, 2002.

54. Volten, H., O. Muñoz, J. W. Hovenier and L. B. F. M. Waters, "An Update of the Amsterdam Light Scattering Database", *Journal of Quantitative Spectroscopy and Radiative Transfer*, Vol. 100, No. 1, pp. 437–443, 2006.

55. Liou, K. N., *An Introduction to Atmospheric Radiation,* Second Edition, Vol. 84 of *International Geophysics*, Academic Press, San Diego, 2002.

56. Mackowski, D. W., "A Multiple Sphere T-Matrix FORTRAN Code for Use on Parallel Computer Clusters Version 3.0", Auburn University Department of Mechanical Engineering, Auburn, AL, United States, 2013.

57. Draine, B. T. and P. J. Flatau, "User Guide for the Discrete Dipole Approximation Code DDSCAT 7.3", arXiv:13056497, 2013.

APPENDIX A: QUANTITATIVE ANALYSIS OF DIFFERENT NECKING MODELS IN PREDICTING THE SCATTERING MATRIX

Additional data for the preliminary problem defined in Section 3.1 is provided in this section. Following subsections include:

- Verification study for generated aggregates based on the simulation results presented in [26],
- A study on the effect of number of fractal-like aggregates generated for the same d_{ve} to reduce the fluctuations on scattering matrix elements due to random nature of fractal generation algorithms,
- A study on the effect of aggregate size distribution sampling on the scattering matrix,
- A study on the effect of refractive index on the scattering matrix in the presence of necking.

A.1. Verification of Aggregate Representations

Scattering matrix elements calculated based on MSTM simulations for the aggregates generated in this study (Section 4.1.1) are compared with the measurement data and MSTM simulation results presented in the study by J. Liu et al. [26]. Accordingly, generated aggregate representations are verified based on the comparison of the MSTM simulation results. Corresponding plots are provided in Figure A.1 below.

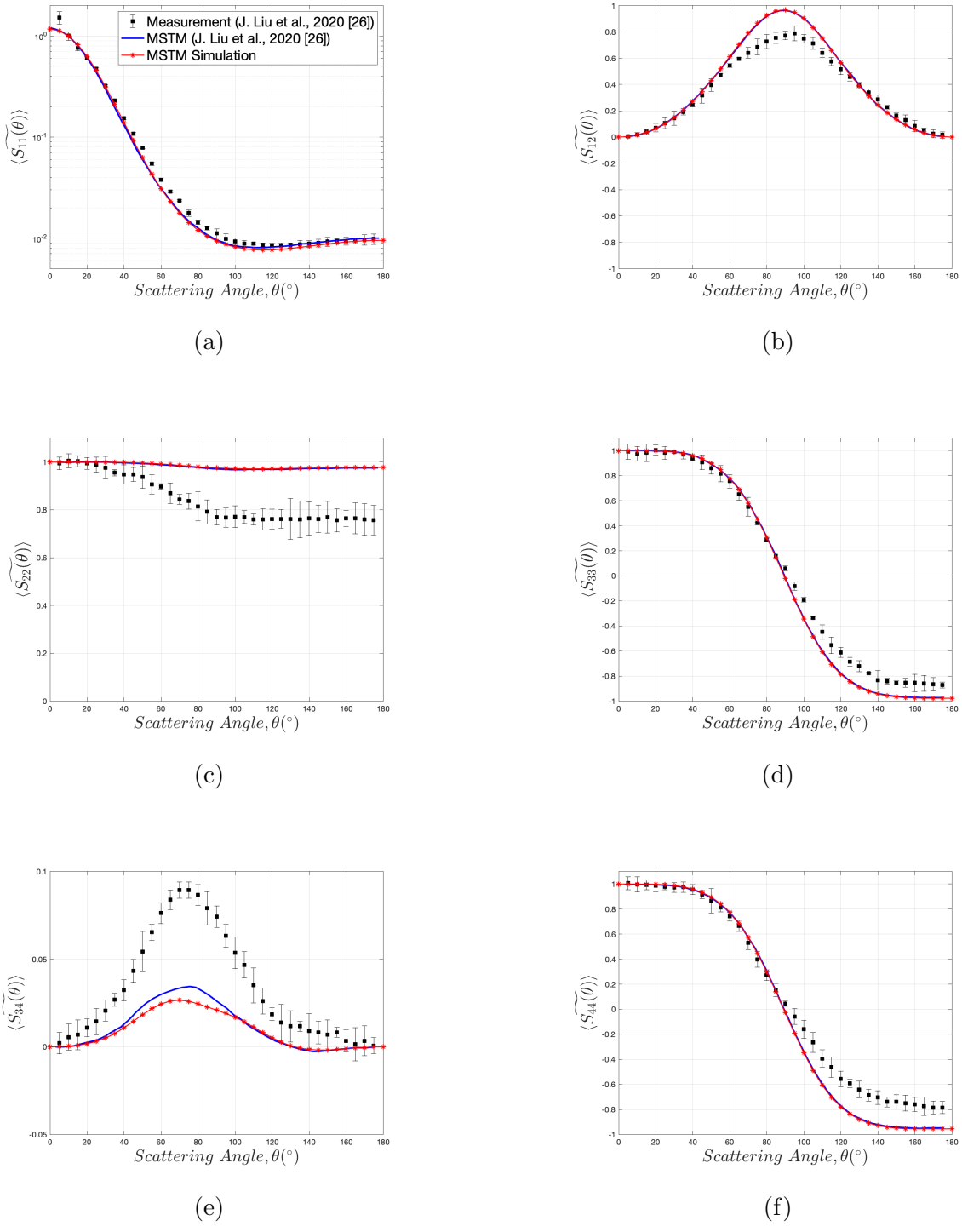

(a) (b) (c) (d) (e) (f)

Figure A.1: Normalized bulk scattering matrix elements obtained from measurement data and MSTM results provided in [26], and MSTM simulations for aggregate representations generated in this study for the monodisperse case.

A.2. Effect of Number of Fractals

The effect of number of fractal-like aggregates generated based on the same d_{ve} to reduce the magnitude of fluctuations in the estimated scattering matrix elements attributed to the random nature of fractal generation algorithms is studied for the monodisperse primary particle case. Mean values of the scattering matrix elements are calculated over different number of fractals, N_{frac}, generated based on the same d_{ve} and the resultant scattering profiles are presented in Figure A.2. As can be seen from Figure A.2, the differences in mean values of the scattering matrix elements are negligible in general. Accordingly, a single fractal representation can be used for the monodisperse primary particle case to reduce the computational load.

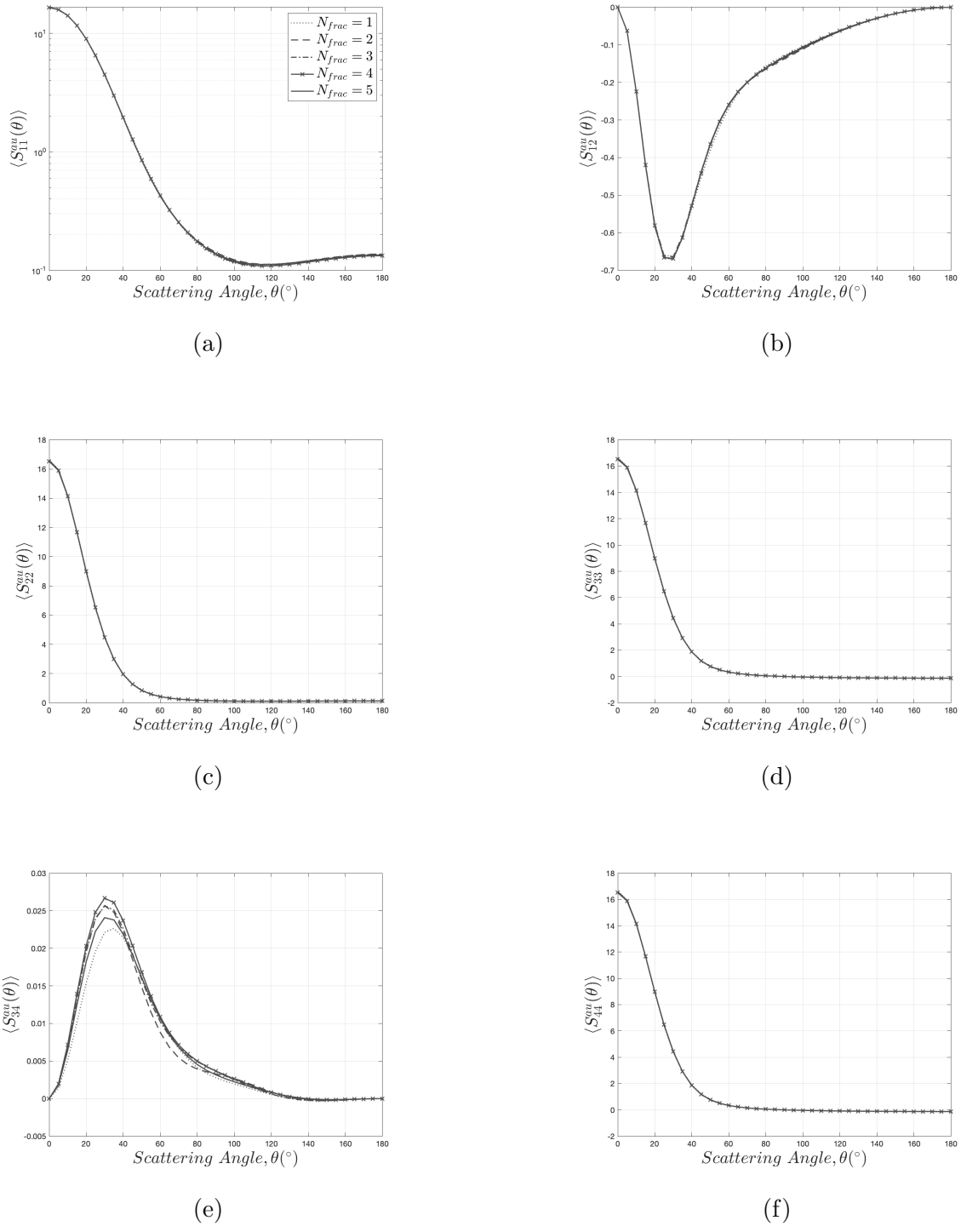

Figure A.2: Mean values of the bulk scattering matrix elements averaged over $N_{frac} = 1$, 2, 3, 4, and 5 for the monodisperse case.

A.3. Effect of Aggregate Size Distribution Sampling

The effect of sampling of the aggregate size distribution defined over d_{mob}, which is then converted to d_{ve}, on the scattering matrix elements is investigated. 4 different d_{ve} samplings are utilized to calculate the bulk scattering matrix elements based on Equation (4.6) provided in Section 4.1.4.1, and the resultant scattering matrix element profiles are shown in Figure A.3. As can be seen from Figure A.3, the differences between scattering matrix element profiles obtained for different samplings are negligible. Therefore, coarse smpling grid with 9 sample d_{ve} points can be used to reduce the computational load.

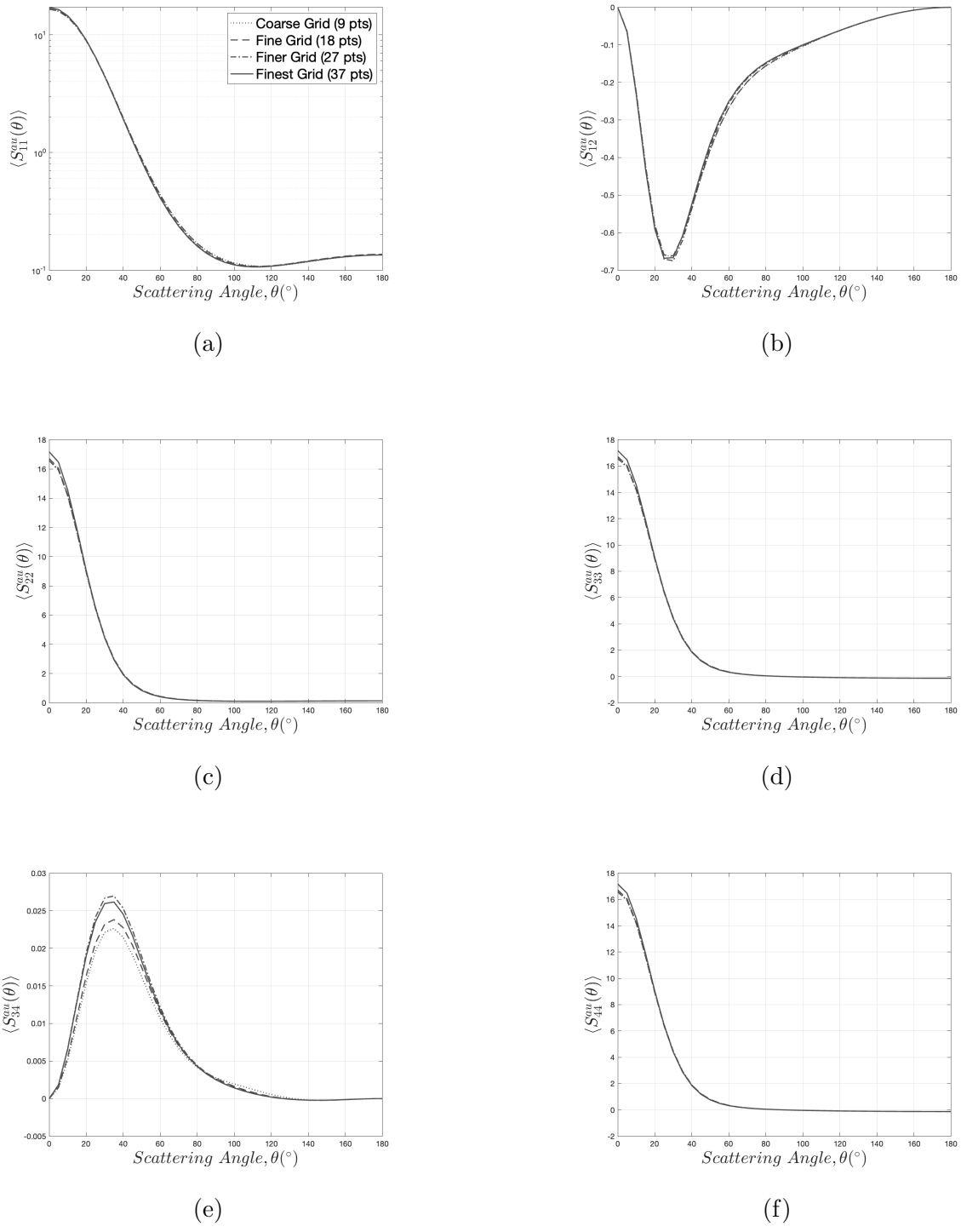

Figure A.3: Bulk scattering matrix elements calculated over different samplings of d_{ve} distribution for the monodisperse case.

A.4. Effect of Refractive Index on the Scattering Matrix of Soot Aggregates Including Necking

The effect of refractive index on the scattering matrix elements in the presence of necking implemented via MCCM with $C_{neck} = 0.8$ is investigated for the monodisperse primary particle case. The real and imaginary parts of the refractive index are altered based on the corresponding limits provided in J. Liu et al. [26], and the corresponding scattering matrix elements are calculated using DDSCAT. The resultant normalized and bulk scattering matrix elements for the considered set of soot refractive indices are shown in Figure A.4 and A.5, respectively. As can be seen from Figure A.4, the impact of refractive index on the normalized scattering matrix elements, especially $\widetilde{\langle S_{22} \rangle}$ and $\widetilde{\langle S_{34} \rangle}$, are considerable. However, its impact is relatively insignificant compared to that of necking. Therefore, relying on the constant refractive index assumption would not significantly change the reliability of the analysis of different necking models in representing the real necking phenomenon in the toluene soot aggregates. Moreover, the impact of refractive index on the bulk scattering matrix elements is observed to be even less significant as can be seen in Figure A.5. Another observation is that the imaginary part of the refractive index has relatively more pronounced impact on the scattering matrix elements as compared to that of the real part in general. Note that the imaginary part of the refractive index is related with the absorption coefficient.

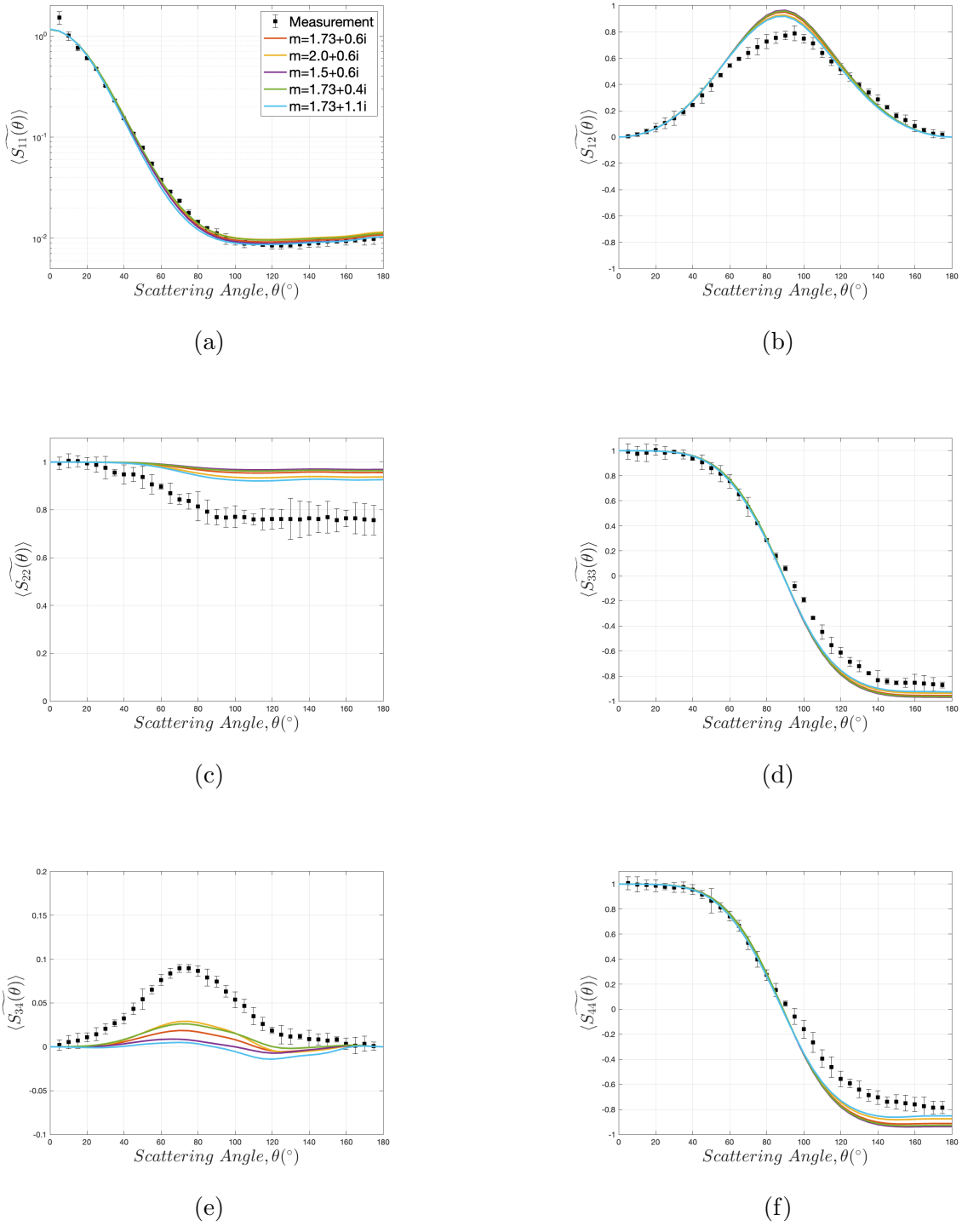

(a) (b) (c) (d) (e) (f)

Figure A.4: Normalized bulk scattering matrix elements calculated for different soot refractive indices for the monodisperse primary particle case with necking implemented via MCCM with $C_{neck} = 0.8$.

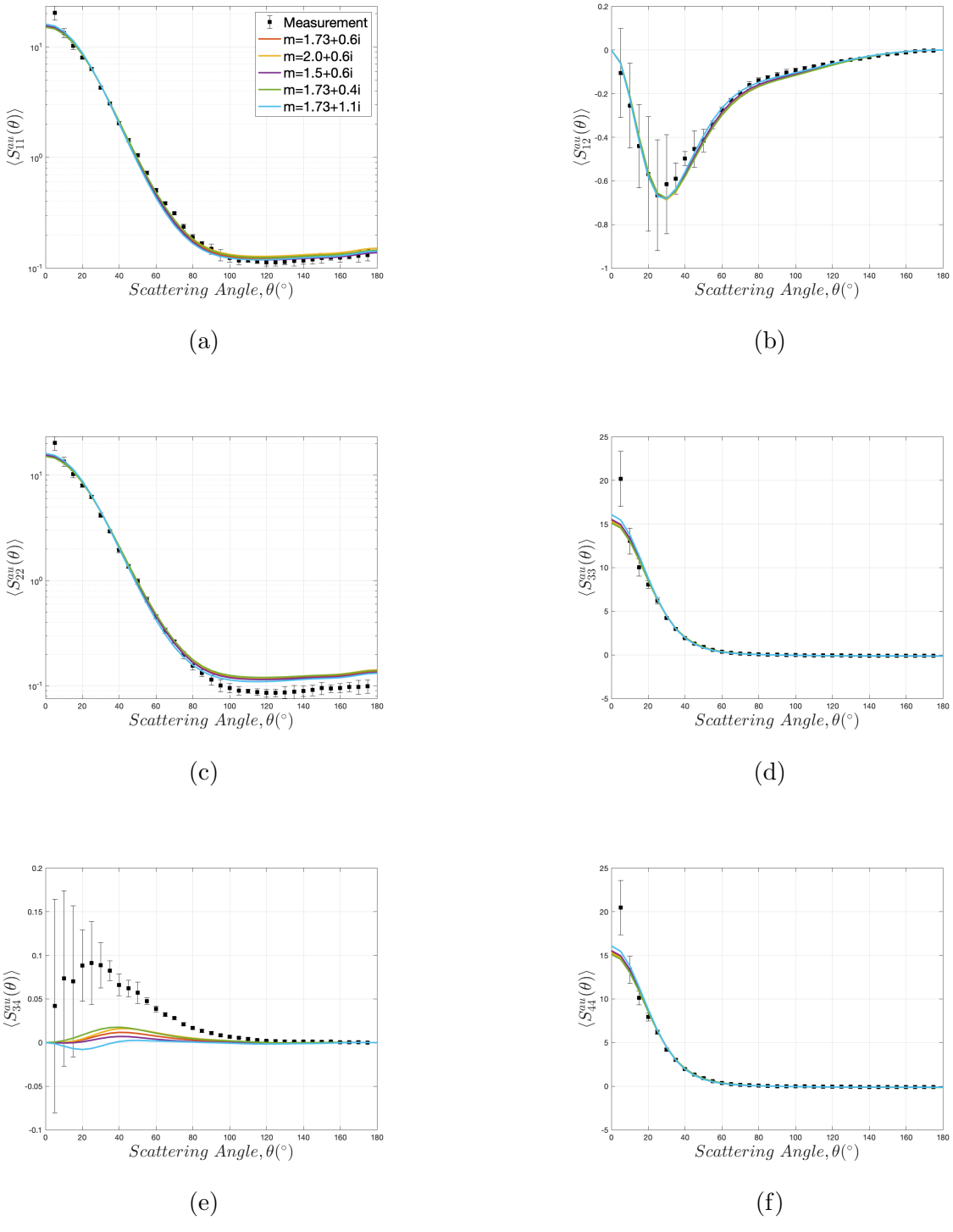

Figure A.5: Bulk scattering matrix elements calculated for different soot refractive indices for the monodisperse primary particle case with necking implemented via MCCM with $C_{neck} = 0.8$.

APPENDIX B: EFFECTS OF NECKING AND POLYDISPERSITY IN AGGREGATE AND PRIMARY PARTICLE SIZE ON THE SCATTERING MATRIX

Additional data related with the problem described in Section 3.2 is provided in this section. Following subsections include:

- A study comparing the scattering matrix elements estimated using MSTM and DDSCAT, which is conducted to ensure the fidelity of DDSCAT simulation results for the specified dipole separation distance and number of target orientations used to calculate the orientation averaged properties,
- A study on the effect of sampling of the aggregate size distribution used to calculate the bulk scattering matrix elements.

B.1. Comparison of Scattering Matrix Elements Estimated by MSTM and DDSCAT

Scattering matrix elements estimated based on MSTM v3.0 [16] and DDSCAT [17] are compared to ensure the fidelity of DDSCAT simulations for the specified dipole separation distance, d, and number of target orientations used to calculate the orientation averaged properties. The bulk scattering matrix elements calculated using MSTM and DDSCAT for aggregates formed by monodisperse primary particles (Case 1) are shown in Figure B.1. The differences between MSTM and DDSCAT simulation results are negligible as can be seen in Figure B.1.

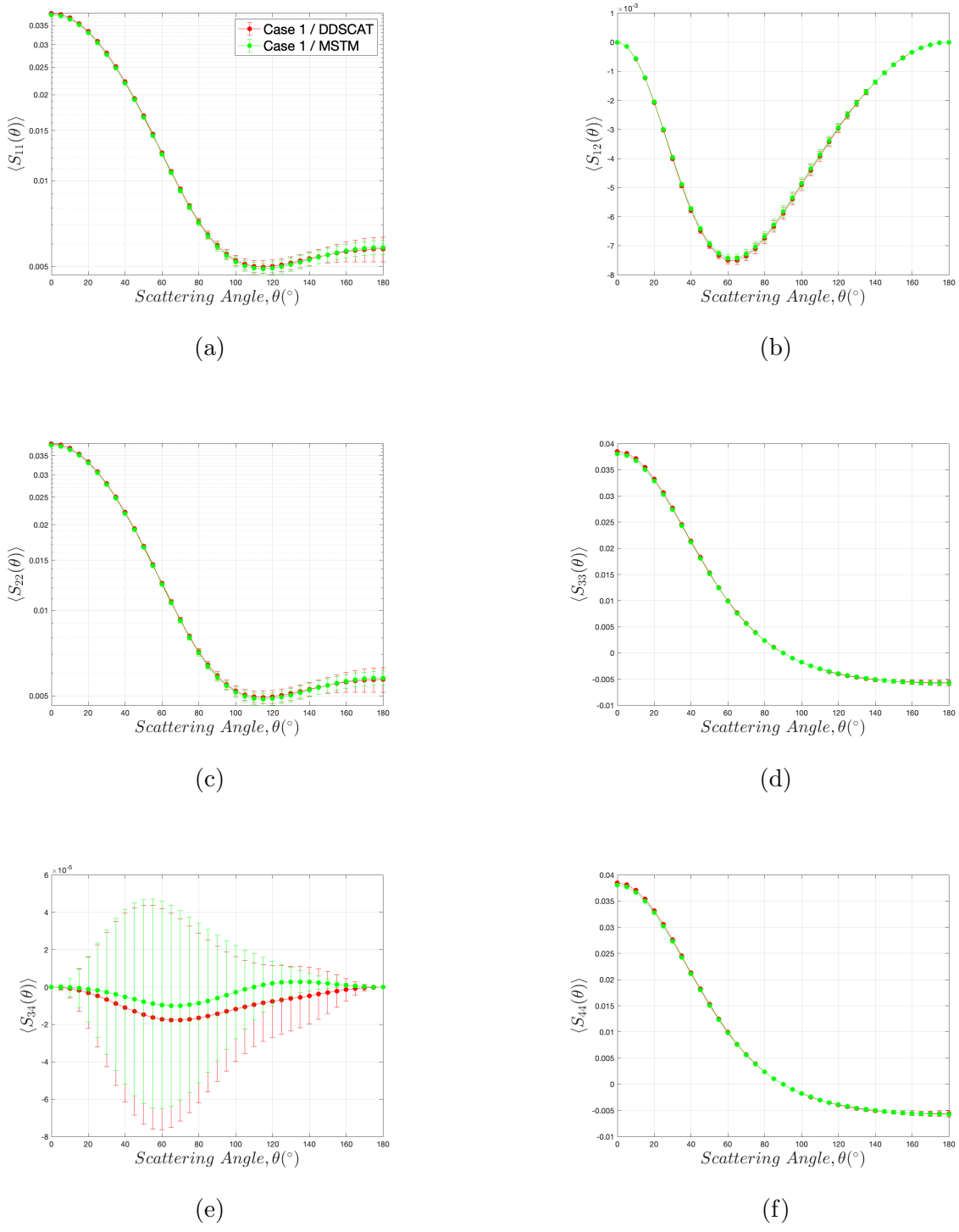

Figure B.1: Bulk scattering matrix elements calculated via MSTM and DDSCAT for aggregate formed by monodisperse primary particles with no necking.

B.2. Effect of Aggregate Size Distribution Sampling

Different samplings of the aggregate size distribution described in Figure 3.1a in Section 3.2 are used to calculate the bulk scattering matrix elements, $\langle S \rangle$ and $\langle S^{au} \rangle$, for the aggregates formed by monodisperse primary particles (Case 7). The impact of sampling of aggregate size distribution on the elements of $\langle S^{au} \rangle$ is demonstrated in Figure B.2. Considerable fluctuations are observed in between the scattering matrix elements for the coarser samplings (Sampling 1, 2, and 3), whereas the corresponding differences between Sampling 4 and 5 become insignificant as can be seen in Figure B.2. Although the differences seem to be considerable in $\langle S_{34}^{au} \rangle$, the magnitudes are relatively small and variances are large such that distinguishing the profiles obtained for different samplings becomes challenging. Overall, Sampling 4 and 5 yield nearly indistinguishable bulk scattering matrix elements. Therefore, increasing the sampling fineness further from Sampling 4 is shown not to yield considerable improvement in the accuracy of the resultant scattering matrix elements.

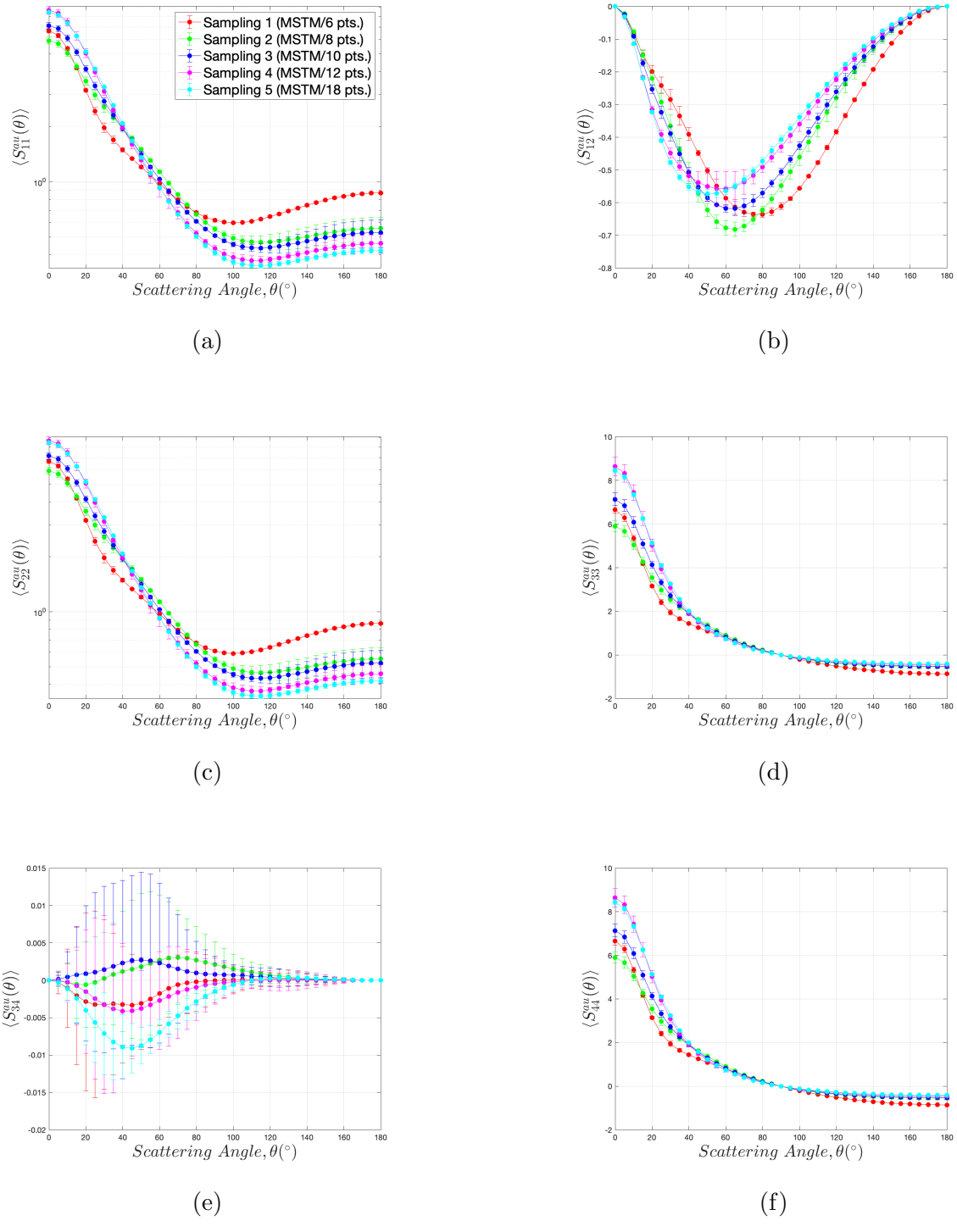

Figure B.2: Bulk scattering matrix elements for different samplings of the aggregate size distribution defined in Figure 3.1a (Section 3.2), for aggregates formed by monodisperse primary particles (Case 7).

APPENDIX C: FURTHER EXPLANATIONS ON THE SCATTERING SIMULATION SOFTWARE

Further explanations regarding the input and output parameter files for the utilized scattering simulation software, DDSCAT and MSTM, are provided in this section.

C.1. Explanations for Input and Output Parameter Files for DDSCAT

DDSCAT by Draine and Flatau [17] uses an input parameter file for estimating the optical properties of target structures which are expressed as a finite array of polarizable points, referred as dipoles. Depending on the geometry of particles/structure, one can use either built-in routines to generate dipoles (if the considered geometry can be expressed by the predefined geometries) or a manual routine necessitating an input file containing the dipole locations representing the target structure. The manual routine is utilized in this study to estimate the scattering properties of aggregate representations including necking since these structures have complex geometries. FROM_FILE is the subroutine of DDSCAT utilized to estimate the scattering properties of structures for which the corresponding array of dipoles is provided manually.

An example input parameter file, `ddscat.par`, for FROM_FILE subroutine that is used to calculate scattering properties of an aggregate representation including necking will be explained. Further details can be found in [57]. First few lines of the input parameter file starts with preliminary specifications for the iterative solution algorithms that are to be utilized in calculating the optical properties of the considered structure. The default specifications are used in the related part of the example input file as provided in Figure C.1.

```
' ========== Parameter file for v7.3 ==================='
'**** Preliminaries ****'
'NOTORQ' = CMTORQ*6 (DOTORQ, NOTORQ)
'PBCGS2' = CMDSOL*6 (PBCGS2, PBCGST, GPBICG, QMRCCG, PETRKP)
'GPFAFT' = CMETHD*6 (GPFAFT, FFTMKL) -- FFT method
'GKDLDR' = CALPHA*6 (GKDLDR, LATTDR, FLTRCD) -- DDA method
'NOTBIN' = CBINFLAG (NOTBIN, ORIBIN, ALLBIN)
```

Figure C.1: Default preliminary specifications in DDSCAT input file.

Then memory allocation is conducted depending on the number of dipoles generated to represent the aggregate. In the following lines, the target geometry and composition is derived from an external file, called `shape.dat`, containing the dipole locations and compositions. The refractive index is read from another external file, `diel`, which includes the file `m1.73_0.6` created to define the refractive index of soot considered in this study. Following lines includes specifications related with the near field calculations which are not of interest in this study since the scattering properties are measured at the far-field. Corresponding lines of the input parameter file is provided in Figure C.2.

```
'**** Initial Memory Allocation ****'
300 300 300 = dimensioning allowance for target generation
'**** Target Geometry and Composition ****'
'FROM_FILE' = CSHAPE*9 shape directive
no SHPAR parameters needed
1         = NCOMP = number of dielectric materials
'../diel/m1.73_0.6' = file with refractive index 1
'**** Additional Nearfield calculation? ****'
0 = NRFLD (=0 to skip nearfield calc., =1 to calculate nearfield E)
0.0 0.0 0.0 0.0 0.0 0.0
```

Figure C.2: Part of the input file of DDSCAT specifying the parameters related with the initial memory allocation, target geometry and composition, and near-field calculations.

An example shape file, `shape.dat`, for an aggregate with 51 primary particles including necking implemented via MCCM with $C_{neck} = 0.6$ which is represented by 119316 dipoles is provided in Figure C.3. The first line in the shape file is a comment line that does not affect the calculations. `NAT` is the number of dipoles generated to represent the aggregate. Note that the dipole locations (`IX`, `IY`, `IZ`) must be integers which express the position with respect to the center of the aggregate in terms of dipole separation distance, d. `ICOMP` denotes the composition of the dipoles which is set as 1 in x, y, and z directions for all dipoles since the considered structure is assumed to be homogeneous and isotropic.

```
>TARCEL: NP fractal with 51 spheres
  119316 = NAT,
1.000000 0.000000 0.000000 = A_1 vector
0.000000 1.000000 0.000000 = A_2 vector
1.000000 1.000000 1.000000 = lattice spacings (d_x,d_y,d_z)/d
-7.00000 29.00000 -36.50000 = lattice offset x0(1-3)
    JA IX IY IZ ICOMP(x,y,z)
     1  -2  26   2 1 1 1
     2  -3  27   2 1 1 1
     3  -2  27   2 1 1 1
     4  -1  27   2 1 1 1
     5  -3  28   2 1 1 1
     6  -2  28   2 1 1 1
     7  -1  28   2 1 1 1
     8  -4  24   3 1 1 1
     9  -3  24   3 1 1 1
    10  -2  24   3 1 1 1
     .
     .
     .
119316 -34  26 -84 1 1 1
```

Figure C.3: Shape file representing a sample aggregate with 51 primary particles including necking implemented via MCCM with $C_{neck} = 0.6$.

The following few lines are specifications related with the iterations, wavelength of the incident light, refractive index of the ambient medium, effective radius of the aggregate (in units of μm), and the polarization states. The specifications used in this study are provided in Figure C.4.

```
'**** Error Tolerance ****'
1.00e-5 = TOL = MAX ALLOWED (NORM OF |G>=AC|E>-ACA|X>)/(NORM OF AC|E>)
'**** Maximum number of iterations ****'
5000     = MXITER
'**** Integration cutoff parameter for PBC calculations ****'
1.00e-2 = GAMMA (1e-2 is normal, 3e-3 for greater accuracy)
'**** Angular resolution for calculation of <cos>, etc. ****'
0.5 = ETASCA (number of angles is proportional to [(3+x)/ETASCA]^2 )
'**** Vacuum wavelengths (micron) ****'
0.532 0.532 1 'LIN' = wavelengths
'**** Refractive index of ambient medium'
1.0000 = NAMBIENT
'**** Effective Radii (micron) **** '
0.0601 0.0601 1 'LIN' = eff. radii
'**** Define Incident Polarizations ****'
(0,0) (1.,0.) (0.,0.) = Polarization state e01 (k along x axis)
2 = IORTH
'**** Specify which output files to write ****'
0 = IWRKSC
```

Figure C.4: Part of the input file of DDSCAT specifying the parameters related with the iterative solutions, wavelength of the incident light, refractive index of the medium, effective radius of the aggregate, and the polarization states.

Then, the target orientations, scattering matrix elements of interest, scattered directions, and number of scattering planes are specified in the remaining part of the input parameter file as in Figure C.5.

```
'**** Specify Target Rotations ****'
0.    360.  10  = BETAMI, BETAMX, NBETA  (beta)
0.    180.   5  = THETMI, THETMX, NTHETA (theta)
0.    360.  10  = PHIMIN, PHIMAX, NPHI (phi)
'**** Specify first IWAV, IRAD, IORI (normally 0 0 0) ****'
0   0   0    = first IWAV, first IRAD, first IORI
'**** Select Elements of S_ij Matrix to Print ****'
6 = NSMELTS = number of elements of S_ij to print (not more than 9)
11 12 22 33 34 44 = indices ij of elements to print
'**** Specify Scattered Directions ****'
'LFRAME' = CMDFRM (LFRAME, TFRAME for Lab Frame or Target Frame)
1 = NPLANES = number of scattering planes
0.  0. 180. 5 = phi, theta_min, theta_max (deg) for plane A
```

Figure C.5: Part of the input file of DDSCAT specifying the parameters related with the target rotations, scattering matrix elements of interest, scattered directions, and number of scattering planes.

There are multiple output files of DDSCAT, whereas the optical properties of interest of this study can be derived from a single output file, named as `w000r000.avg`. This file, contains information of the integral optical properties such as the scattering cross-section as well as the scattering matrix elements. Note that these elements are associated with the scattering matrix, S. Accordingly, derivation of the elements of S^{au} requires post-processing (proper scaling by $C_{sca}k^2/4\pi$). The section of the output file, `w000r000.avg`, that contain the estimated optical properties is provided in Figure C.6.

```
         Qext        Qabs        Qsca      ...        Qpha
JO=1:  9.0710E-01  8.2755E-01  7.9561E-02  ...    6.3351E-01
JO=2:  9.0709E-01  8.2756E-01  7.9549E-02  ...    6.3352E-01
mean:  9.0709E-01  8.2756E-01  7.9555E-02  ...    6.3352E-01
Qpol=  9.6560E-06                         dQpha= -8.4639E-06
.
.
.
            Mueller matrix elements
 theta    phi    Pol.    S_11        S_12        ...   S_44
  0.00   0.00  0.00000  3.8571E-02  9.5621E-09  ...  3.849E-02
  5.00   0.00  0.00380  3.8218E-02 -1.4509E-04  ...  3.814E-02
 10.00   0.00  0.01524  3.7181E-02 -5.6671E-04  ...  3.710E-02
    .
    .
    .
 180.00   0.00  0.00000  4.7493E-03  9.1052E-10 ... -4.627E-03
```

Figure C.6: Part of the output file of DDSCAT containing the estimated optical properties of the target structure.

C.2. Explanations for Input and Output Parameter Files for MSTM v3.0

MSTM v3.0 by Mackowski and Mishchenko [16] uses an input parameter file to estimate the scattering properties of a cluster of spherical particles. An example input parameter file for a cluster of 22 spherical polydisperse primary particles generated based on FracVAL by Moran et al. [41] is explained in this section. Further details can be found in [56]. Note that $N_p = 22$ is a sample point selected from the aggregate size distribution specified in Section 3.2.

First few lines of the corresponding input file specify the number of particles in the cluster, particle position and radii (derived from FracVAL), name of the output file which will contain the estimated scattering properties, an integer switch which writes the properties for individual spheres as well to the output file when specified as 1, and the length scale factor ($k = 2\pi/\lambda$) which scales the dimensions of the aggregate based on the wavenumber. Note that the dimension of the wavelength implemented in the length scale factor must be consistent with the dimensions of the primary particle center locations and radii provided in the input position file. Corresponding lines for the specified case are provided in Figure C.7. The input parameter file is organized as consecutive lines, where the first line is the input parameter name and the following is the specified input. A position file is specified in line 4 to import the position and radius information of the aggregate composed of 22 polydisperse primary particles. The position file, `Np22_rpg15.46_spg1.36_v1.pos`, contains data in the form of a 22×4 matrix, where the first column contains primary particle radii and the remaining columns correspond to x, y, and z coordinates of the particle centers in order.

The following lines are provided in Figure C.8, which specify the refractive indices of particles and the medium. Corresponding parameters are specified according to the problem description given in Section 3.2.

```
number_spheres
22
sphere_position_file
Np22_rpg15.46_spg1.36_v1.pos
output_file
Fout_Np22_rpg15.46_spg1.36_v1.dat
write_sphere_data
1
length_scale_factor
0.011810d0
```

Figure C.7: First part of the input file for MSTM specifying the parameters related with the number, position, and radius of primary particles in the aggregate, and the length scale factor.

```
real_ref_index_scale_factor
1.730d0
imag_ref_index_scale_factor
0.600d0
real_chiral_factor
0.0d0
imag_chiral_factor
0.0d0
medium_real_ref_index
1.0d0
medium_imag_ref_index
0.d0
medium_real_chiral_factor
0.d0
medium_imag_chiral_factor
0.d0
```

Figure C.8: Part of the input file of MSTM specifying the parameters related with the refractive indices of particles and the medium.

Remaining lines of the input parameter file contains specifications regarding the solution methodology and iterations for which the default values can be used. Important parameters that need to be specified for this study in the remaining lines of the parameter file are provided in Figure C.9. Scattering matrix elements will be presented from 0° to 180° with 5° increments based on these specifications. Note that the calculated scattering matrix elements are associated with S^{au}. Scattering matrix is not normalized since the corresponding integer switch is set to 0. If it is set to 1, scattering matrix elements other than S_{11}^{au} are normalized by $S_{11}^{au}(\theta)$. Finally, incident azimuthal and polar angles are specified to be consistent with the definitions by DDSCAT.

```
min_scattering_angle_deg
0.0d0
max_scattering_angle_deg
180.d0
delta_scattering_angle_deg
5
normalize_scattering_matrix
0
fixed_or_random_orientation
1
incident_azimuth_angle_deg
0.d0
incident_polar_angle_deg
90.0d0
```

Figure C.9: Part of the input file of MSTM containing specifications of the remaining significant parameters required for this study.

Corresponding output file contains information regarding the optical properties such as extinction, absorption, and scattering cross-sections, the asymmetry factor, the scattering matrix (S^{au}), and the scattering matrix expansion coefficients. Therefore, post-processing (proper scaling by $C_{sca}k^2/4\pi$) is required to calculate the elements of S from the output file of MSTM. Few lines from the corresponding output file providing information about the specified optical properties are presented in Figure C.10.

```
total ext, abs, scat efficiencies, w.r.t. xv, and asym. parm
 0.71077E+00  0.65515E+00  0.55625E-01  0.20773E+00
scattering matrix elements
  theta      11           12           13        ...       44
   0.00  0.24285E+01  0.00000E+00  0.00000E+00   ...   0.24156E+01
   5.00  0.24143E+01 -0.90743E-02 -0.36633E-06   ...   0.24013E+01
  10.00  0.23721E+01 -0.35796E-01 -0.14867E-05   ...   0.23590E+01
     .
     .
     .
 180.00  0.84742E+00 -0.32063E-14 -0.10382E-17   ...  -0.83524E+00
```

Figure C.10: Part of the output file of MSTM containing the optical properties of the target structure.